Ultra-long-distance transport of aeolian sand: the provenance of an intermontane desert, SE China

Shuo Cao[1], Laiming Zhang[1], Nigel P. Mountney[2], Jing Ma[3], Mingang Hao[1], and Chengshan Wang[1]

[1]*State Key Laboratory of Biogeology and Environmental Geology, and School of Earth Sciences and Resources, China University of Geosciences (Beijing), Beijing 100083, China.*

[2]*Fluvial, Eolian & Shallow-Marine Research Group, School of Earth and Environment, The University of Leeds, LS2 9JT, UK.*

[3]*Institute of Mineral Resources Research, China Metallurgical Geology Bureau, Beijing 101300, China.*

ABSTRACT

Intermontane deserts are an important type of arid-climate sedimentary system. Although rare at present, the sedimentary records of intermontane deserts reveal their widespread development in past greenhouse periods, and they might develop in the near future in response to ongoing global warming. Determination of the provenance of sand supplied for the construction of intermontane deserts is important to gain improved understanding of the potential impact of future climate on environmental evolution in arid and semi-arid regions. During the Cretaceous, a typical intermontane desert developed in the Xinjiang Basin, southeast China. In this study, the origin, spatial variability, and transport pathways of both aeolian and alluvial-fluvial sediments in the

Xinjiang intermontane desert are investigated by analyses of bulk-rock petrography and detrital-zircon U-Pb geochronology. Our results demonstrate that the sand in the Xinjiang intermontane desert succession was mainly of extraneous origin and wind-derived. The nearby South China Block and South China Magmatic Belt were primary sources, and the 1000 km-distant western margin of Yangtze Block was an important secondary source. During the Late Cretaceous, the westerlies were stronger in the northern than in the southern hemisphere with doubled wind speeds. In such a climatic context, our results suggest that the ultra-long-distance aeolian sediment transport was likely further enabled by two factors: (i) the strengthening of intermittent westerly winds during short-lived glacial episodes; (ii) the presence of a low-relief corridor that served as a transport pathway from source to sink.

Keywords: intermontane desert; provenance analysis; U-Pb zircon ages; sand supply mechanism; ultra-long-distance transportation

INTRODUCTION

At present, approximately 30% of the Earth's land surface is covered by climatic deserts, making them one of the most important terrestrial sedimentary environments (Brookfield and Silvestro, 2010; Mountney, 2006; Rodríguez-López et al., 2014). On the basis of geomorphic features, these dryland regions can be divided into shield-platform deserts and intermontane deserts (Cooke et al., 1993; Whitford and Duval, 2019); the latter type is the subject of this study. Shield-platform deserts develop across tablelands and basin lowlands bordered by ancient mountains. This type of desert is widespread today and their preserved successions are widely identified in the ancient rock record (e.g., Rodríguez-López et al., 2014; Rittner et al., 2016; Dickinson and Gehrels, 2003). In contrast, intermontane deserts develop and accumulate principally in valleys and structural depressions that are typically confined by geologically younger mountain ranges (Cooke et al., 1993; Whitford and Duval, 2019). Today, relatively few intermontane deserts are developed; notable examples are present in the Basin and Range Province of the Western United States. Typical intermontane deserts tend to be relatively less sandy, and are commonly called steppe-deserts, such as in Patagonia. Despite being of limited number and extent today, the sedimentary records of preserved examples of intermontane deserts are many, and their development was apparently especially widespread during past greenhouse periods (Barbolini et al., 2020; Brookfield, 1980; Cao et al., 2020; Chen et al., 2008; Jiang et al., 1999; Jiao et al., 2020; Li et al., 2018b; Walker et al., 2002; Yu et al., 2020). For example, many sand-prone intermontane deserts are known to have developed in Asia during greenhouse conditions during the Cretaceous in response to worldwide desertification (Cao et al., 2020; Chen et al., 2019; Li et al., 2018a; Li et al., 2018b; Wu et al., 2017; Wu et al., 2018; Yu et al., 2020).

In the near future, as mean global atmospheric CO_2 concentrations continue to rise, it is predicted that the Earth may enter a prolonged greenhouse state, similar to that experienced during the Cretaceous (Caesar et al., 2013; Intergovernmental Panel on Climate, 2014). Given that the onset of desertification is markedly influenced by climatic change (Brookfield and Silvestro, 2010; Mountney, 2006), it is important to assess how and where intermontane deserts might begin to develop in the near future. This study addresses this challenge by examining sedimentary evidence to reveal the mechanisms of formation a Cretaceous intermontane desert succession. Results of this study are valuable for forecasting the potential development of intermontane deserts in the near future.

Assessment of the provenance of sediment (i.e., sediment sources and transport pathways) is essential for understanding the processes of aeolian sediment transport and deposition, and for assessing the sediment state of an aeolian system (Du et al., 2018; Kocurek and Lancaster, 1999; Muhs et al., 2017; Williams, 2015). Provenance analysis provides valuable information to support further sedimentological, geomorphological, and palaeoclimatological studies (Jiang and Yang, 2019). Determination of the provenance of desert sediments has been a major focus of numerous recent aeolian studies (e.g., Lancaster et al., 2013; Zhang et al., 2020), and has been important to improve understanding of how and why large accumulations of aeolian sediments are developed and preserved (Bertolini et al., 2020; Dickinson and Gehrels, 2003, 2009). Previous studies of aeolian sediment provenance have hitherto mainly been conducted for shield-platform deserts. Such studies have demonstrated that the aeolian deposits typically comprise both endogenous sands generated by wind erosion of surrounding local bedrock (e.g., parts of the Sahara Desert) and exogenous sands supplied by external or adjacent rivers (e.g., the Namib Desert) (Garzanti et al., 2014; Zhang et al., 2020; Bertolini et al., 2020). However, the provenance of sand supply to intermontane deserts remains relatively poorly understood.

The aim of this paper is to reconstruct sediment transportation to (and within) an intermontane desert developed during a greenhouse period. Recently, a Mid-Late Cretaceous intermontane desert has been identified in the Xinjiang Basin, Southeastern China (Wu et al., 2018a; Jiang et al., 2008) (Fig. 1). Within the preserved succession of this intermontane desert system, analyses of indicators of palaeowind and subaqueous palaeocurrents have demonstrated that the formative aeolian and fluvial flows were oriented in opposing directions (Cao et al., 2020). This partitioning of wind- and river-derived sediments is conducive to studying aeolian sand supply. In this study, the origin, spatial variability, and transport pathways of both aeolian and alluvial-fluvial sediments in the Xinjiang intermontane desert are investigated by combining bulk-petrography analyses and detrital-zircon U-Pb geochronology. Results additionally provide constraints on palaeoclimate and palaeogeography.

GEOLOGICAL SETTING

The South China Block (SCB) comprises the Yangtze Block (YB) to the northwest and the Cathaysia Block (CB) to the southeast (Fig. 1); each of these blocks has distinctive crustal ages and tectonic histories (Yan et al., 2011; Duan et al., 2011). In response to Cretaceous lithospheric extension in the SCB, a series of terrestrial rifted basins that collectively represent the Late Mesozoic Basin and Range System developed between the YB and the CB (Wang and Shu, 2012; Chen et al., 2017; Shu et al., 2009). During the Mid-Late Cretaceous, many deserts developed in these intermontane basins under the influence of a subtropical high-pressure belt (Cao et al., 2020; Chen et al., 2019; Chen et al., 2008; Jiang et al., 1999; Li et al., 2018a; Li et al., 2018b; Wu et al., 2017; Wu et al., 2018; Yu et al., 2021a). As a representative of these intermontane basins, the Xinjiang Basin accumulated a >6000 m-thick succession of red beds (Guo et al., 2013). Within the overall red-bed succession, a >400 m-thick sequence of aeolian-dominated strata comprising dune-set, interdune, and sandsheet architectural elements has been recognized; this has been interpreted as the sedimentary record of an intermontane desert (Cao et al., 2020; Wu et al., 2018a).

The Xinjiang Basin covers an area of over 3600 km^2; this elongate basin is 130 km E-W and 30 km N-S (Cao et al., 2020). The basin is located in the central part of the Ganhang tectonic belt, which is itself located at the junction of the YB and the CB (Fig. 1B). The basin is fringed by the Jiangnan Orogen (JNO) to the northwest and by the South China Magmatic Belt (SCMB) to the southeast; these two uplifted regions were the closest potential substantial sediment sources that may have contributed to the basin fill, and each of them has distinctive magmatic rock ages (Cawood et al., 2018). The JNO is characterized by an abundant population of relatively younger zircons (~700-800 Ma), and two populations of older zircons (~1550-2000 Ma and ~2300-2600 Ma) (Li et al., 2018). By contrast, the SCMB is characterized by abundant zircons with an age of ~80-300 Ma (Yan et al., 2011).

From bottom to top, the stratigraphic units of the Xinjiang Basin are the Lower Cretaceous Huobashan Group and the Upper Cretaceous Guifeng Group (Xi et al., 2019) (Fig. 2). Due to an absence of both age-diagnostic fossils and of datable volcanic ash layers, there are no direct absolute age constraints for the overall succession. Deposits of the Guifeng Group have been interpreted as the preserved succession of a typical intermontane desert (Cao et al., 2020). It is subdivided into the basal Hekou Formation (K_2h), the middle Tangbian Formation (K_2t), and the topmost Lianhe Formation (K_2lh). The Hekou and Lianhe formations (each 2000–3000 m thick) are mainly composed of thick- to very thick-bedded purple-red conglomerates and sandy conglomerates with a lesser amount of thin- to medium-bedded sandstones, siltstones, and mudstones. These formations represent alluvial-fan and braided-stream palaeoenvironments (Guo et al., 2013). Between the above-mentioned two formations, the middle Tangbian Formation (~500 m thick) is characterized by brick-red, fine- to medium-grained, well-sorted massive quartz sandstones with well-developed large-scale (ca. 5-10 m thick) simple sets that are internally characterized by high-angle-inclined cross-bedding. Before correction to negate any component of tectonic tilt, the maximum foreset dip angles are ~35° to 42°; following restoration, the maximum foreset dip angles are ~29° to 36°. These deposits have been interpreted to be of aeolian dune origin (Chen et al., 2016; Wu et al., 2018a).

According to the previous studies of aeolian deposits in the Sichuan Basin (Jiang et al., 1999) and the Jianghan Basin (Yu et al., 2021b) to the west of the Xinjing Basin (Fig. 1), the regional wind patterns in the SCB were dominated by westerlies during the Mid-Late Cretaceous: the dominant prevailing wind blew along the elongate axis of the Xinjiang Basin (Cao et al., 2020; Wu et al., 2018). The sedimentary record of west-to-east aeolian sand transport is recorded by the overall orientation of foresets within cross-bedded aeolian dune architectural elements in the Tanbiang succession (Fig. 1).

These dip-azimuths of the foresets of the aeolian dune-set deposits are indicators of the palaeowind direction because Cao et al. (2020) and Wu et al. (2018) have demonstrated that the formative dunes were perfectly transverse (*sensu* Rubin and Carter, 2006) barchanoid dunes. The mean foreset dip-azimuths of cross-beds of these perfectly transverse dunes are distributed unimodally (see Supplementary S1 for details). Based on the above observations, the average wind direction archived by the mean foreset-dip azimuths is oriented to the ENE (vector mean=074°) (Fig. 1 and Fig. S2). Thus, the mean sediment transport in the Xinjiang intermontane desert was affected by westerlies during the Mid-Late Cretaceous (Fig. S2). By contrast, the palaeocurrent directions reconstructed from cross-bedded foresets of alluvial-fluvial architectural elements suggest an overall east-to-west (vector mean=278°) aqueous sediment transport in the Xinjiang Basin (Fig. 1) (Cao et al., 2020; Wu et al., 2018a).

DATA AND METHODS

Sediment Samples

For this study, 14 sandstone samples were collected along a west-to-east transect across the Xinjiang Basin (Fig. 1): four samples of fluvial-alluvial affinity were collected from the Hekou and Lianhe formations; ten samples of aeolian affinity were collected from the Tangbian Formation. Five of the 10 aeolian samples were from deposits of aeolian barchan and transverse dune origin and these were collected from the intermontane desert-centre setting; the other 5 aeolian samples were collected from the desert-margin setting, and are of barchan dune (2), dry interdune (2), and sandsheet

(1) origin (see Table S1 for detail information of location and dune type of each sample).

Palaeocurrent Indicators

One-thousand-five-hundred-and-thirty dip-azimuth readings were measured from 366 separate aeolian dune sets that are themselves interpreted to be the preserved products of perfectly transverse (barchanoid) aeolian bedforms (Cao et al., 2020; cf. Rubin & Carter, 2006). These data have been used to reconstruct palaeo-bedform migration directions, and thereby palaeowind direction. The mean reconstructed wind direction was ENE (vector mean=074°), which reflects the influence of dominant westerlies (Fig. 1).

For the strata of alluvial-fluvial origin, fifty-four palaeocurrent readings were measured from imbricated clasts present in 10 separate sets. In addition, 48 readings were measured from the orientation of elongate trough axes of trough cross-beddings seen in plan view present in 11 separate sets. The mean vector orientation of these 102 readings is 278°, and the spread in the data indicates that the palaeocurrent directions ranged from NW to SW, with flow away from the surrounding mountains toward the centre of the intermontane basin (Fig. 1) (Cao et al., 2020; Wu et al., 2018a).

Petrography

Bulk sand samples were impregnated with araldite epoxy, cut into standard thin sections, and analyzed by counting at least 300 points (grains) under the petrographic microscope. Following the Gazzi-Dickinson point-counting method, every individually analyzed grain was checked to ensure that it was larger than 62.5 μm (cf. Ingersoll et al., 1984; Dickinson, 1985). Sandstone classification has been undertaken based on the relative abundance of three main framework components: quartz (Q), feldspars (F), and lithic fragments (L), and is displayed on a standard Q-F-L ternary diagram (cf. Garzanti, 2019). For lithotype naming, as per convention, the less abundant component is stated first, then the more abundant ones (e.g., litho-feldspatho-quartzose composition translates into Q > F > L > 10% QFL).

Aeolian sediments commonly exhibit distinctive grain size, shape, and sorting characteristics. Many aeolian sandstones are characterized by very-fine to medium sand that is well or very-well sorted, and with grains that are rounded to subangular (Lindholm, 2012; Mountney, 2006). The majority of grains have a thin coating (surface veneer) of iron oxides. Quartz is commonly dominant, and aeolian sandstones mostly plot in the quartzose (Q), feldspatho-quartzose (FQ), litho-feldspatho-quartzose (lFQ), feldspatho-litho-quartzose (fLQ), and litho-quartzose (LQ) fields (Muhs, 2004; Garzanti, 2019). In contrast, alluvial-fluvial sediments range from extremely coarse conglomerates to fine muds. In these sediments, the sand components are typically characterized by very-fine to coarse sand grains that are poorly sorted, many of which are subangular to angular (Chen et al., 2017). Alluvial-fluvial sandstones mostly plot in the quartzo-litho-feldspathic (qLF), quartzo-feldspatho-lithic (qFL), feldspatho-quartzo-lithic (fQL), feldspatho-litho-quartzose (fLQ), litho-feldspatho-quartzose (lFQ), and litho-quartzo-feldspathic (lQF) fields (Lugli et al., 2007).

Detrital Geochronology

In this study, 6 sandstone samples were analyzed by detrital-zircon U-Pb geochronology. Each sample (2 kg) was crushed to 40-60 mesh (i.e., 250-380 μm grain diameter). Conventional magnetic and heavy liquid separation techniques were then used to extract a zircon-rich heavy mineral concentrate (Du et al., 2015). For each sample, a total of 250-300 zircon grains were hand-picked under a binocular microscope. Zircon grains were mounted in epoxy resin and polished to about half their thickness for analysis. Cathodoluminescence (CL) images were taken for all the samples, using a CAMECA electron microprobe, to identify internal textures and choose potential target sites for U-Pb analyses.

For each sample, 100 zircons were randomly selected and analyzed. Zircon U-Pb analyses were carried out following the laser ablation inductively coupled plasma mass spectrometry (LA-ICP-MS) methodology in a microanalysis laboratory affiliated with the State Key Laboratory of Geological Processes and Mineral Resources, China University of Geosciences, Beijing. The laser sampling was performed using a Coherent GeoLasPro 193 nm system. A Thermo Fisher X-Series 2 ICP-MS instrument was used to acquire ion signal intensities. All data were acquired from zircon samples in a single spot ablation mode with a spot size of 32 μm and frequency of 6 Hz. Reference and internal zircon standards 91500 and SRM610 were used for instrument calibration, respectively. Off-line selection and integration of background and analyte signals, as well as time-drift correction and quantitative calibration for trace element analyses and U-Pb dating, were performed using ICPMSDataCal (Wu et al., 2018b).

Common lead was corrected using the LA-ICP-MS common lead correction procedure (ver. 3.15) (Andersen, 2002). Isoplot/Ex (version 4.15) computer software was used for data reduction and to produce the concordia diagrams with 1 σ uncertainty (Ludwig, 2003). U-Pb ages from the zircon grains were calculated by one of two systems: $^{207}Pb/^{206}Pb$ age for older (>1 Ga) zircons and $^{206}Pb/^{238}U$ for younger ones. Ages that have more than ±10% discordance were excluded from the subsequent analysis.

RESULTS

Sandstone Petrography

All the aeolian sandstone samples analysed are quartz-rich and characterized by fine- to medium-grained, moderate to well-sorted, subrounded to subangular grains. Quartz clasts are the most abundant constituent in these samples, constituting 57%–81% (average 75%) of the framework. Predominant monocrystalline quartz grains exhibit undulatory or blocky extinction; they account for 71% of the total quartz grains, on average (Fig. 3). The majority of the feldspar clasts are plagioclase (80%), with a lesser amount of potassium feldspar clasts (20%). In contrast to the aeolian sandstones, the sandstones of alluvial-fluvial origin mainly consist of medium- to coarse-grained, poorly sorted, subangular to angular grains. Of these samples, three contain ~44% lithic fragments, ~52% quartz clasts, and ~4% feldspar clasts, on average; the remaining sample contains ~25% lithic fragments, ~49% quartz clasts, and ~26% feldspar clasts (Fig. 3).

In the QFL diagram (Fig. 3E), all sandstone samples of aeolian origin plot in the litho-quartzose field, although one sample has a relatively higher proportion of lithic components. For the sandstone samples of alluvial-fluvial origin, two plot in the litho-quartzose field, one in the quartzo-lithic field, and one plots at the boundary of the litho-feldspatho-quartzose (lFQ) and feldspatho-litho-quartzose (fLQ) fields (Fig. 3E).

Detrital Zircon Morphology

The zircons in aeolian samples YT-03 and YT-08 (desert-centre setting) are 80–120 μm in length with aspect ratios between 1:1 and 2:1. They are dominantly moderately to well-sorted, rounded to subrounded grains that are subspherical to elongate in shape, and brown, reddish-brown, or grey in colour (Fig. 4). The zircons in aeolian samples YT-07 and YT-13 (desert-margin setting) are 100–150 μm in length with aspect ratios between 1.5:1 and 3:1. They mainly share the same characteristics as the desert-centre zircons, although ~25% of them are prismatic, sub-angular fragmented, and relatively larger (120-150 μm in length) (Fig. 4).

Compared to those in the samples of aeolian origin, the zircons in the samples of alluvial-fluvial origin (YT-12 and YT-14) have a higher proportion of fragmented and euhedral grains, which account for ~88% of all the grains. These zircons are larger (50–200 μm in length), have aspect ratios between 2:1 and 4:1, are mainly subangular to angular, and are moderately or poorly sorted (Fig. 4).

All the zircon grains, from samples of both aeolian and alluvial-fluvial origin, vary from subspherical to elongate in shape and exhibit varied colours. There is no systematic correlation among shape, colour, angularity, and U-Pb ages.

Detrital Zircon Geochronology

The Th/U ratios of zircons generally reflect their origins (Maas et al., 1992). The metamorphic zircons typically have low Th/U ratios (<0.1), whereas magmatic zircons mostly have higher Th/U ratios (0.2 to 1.0) (Kinny et al., 1990). In this study, approximately 95% zircons from the Xinjiang Basin have high Th/U ratios (>0.2) (Fig. S3), which suggest magmatic origins.

In this study, for each sample, 84–95 grains of the 100 grains counted were evaluated to be valid. A total of 367 and 172 zircon grain U-Pb ages were obtained from the sandstone samples of aeolian and alluvial-fluvial origin, respectively. All valid results are plotted on the Concordia curve and give high concordant ages (Fig. 5). Figure 6 shows the relative age-probability plots and the spectra of U-Pb ages for all the samples. The ages of all the samples could be grouped into seven clusters: 98–217 Ma, 220–323 Ma, 328–482 Ma, 503–722 Ma, 732–1386 Ma, 1426–2174 Ma, and 2210–2701 Ma. For each sample, the proportions of age clusters are different. In addition to the clusters referred to above, two older grain populations with ages of 2834 Ma and 3240 Ma were identified in sample YT-07 (Fig. 5).

The seven main U-Pb age clusters are recognized in all the aeolian samples. The 4^{th} cluster (503–722 Ma) is exclusive to the aeolian samples, and the 5^{th} cluster (732–1386 Ma) represents the largest proportion (30-40%). However, the proportions of age clusters are different between samples from the central and the marginal settings of the intermontane desert (Fig. 6). The proportion of the 1^{st} cluster (98–217 Ma) is lower in the desert-centre setting (3–10%) than that in the desert-margin setting (16%). The 6^{th} and 7^{th} clusters (1426–2174 Ma and 2210–2701 Ma) together occupy a higher proportion in the desert-centre setting (31–43%) than those in the desert-margin setting (16–21%). For the sandstone samples of alluvial-fluvial origin, six age clusters are recognized in sample YT-12 and five age clusters are recognized in sample YT-14 (Fig. 6). As the highest age population, the 1^{st} cluster (98–217 Ma) accounts for 61~68%. The 5^{th} cluster (732–1386 Ma) is the second-highest population and accounts for 14–17%, which is less than those of the sandstone samples of aeolian origin. For the other four age clusters, each of them accounts for <8%, which are excluded from detrital zircon geochronology analysis for the alluvial-fluvial samples (Gehrels, 2012; Yan et al., 2011).

Youngest Detrital Zircon Ages

Due to the absence of age-diagnostic fossils and volcanic layers, the age of the intermontane desert is poorly constrained. The zircon U-Pb geochronology could provide a constraint on maximum depositional age (MDA) for each sample. Table 1 presents five MDA candidates for each sample, and the chosen MDA in this study is constrained by YC1σ (2+). The Guifeng Group, which consists of the Hekou, Tangbian, and Lianhe formations, yields a MDA of ca. 109.5–99.5 Ma. Therefore, the maximum depositional age (i.e., ca. 109.5–99.5 Ma) reveals that the intermontane desert formed no earlier than the mid-Cretaceous. Our age constraint is consistent with Li et al. (2019)

who suggested that the Guifeng Group is Cenomanian-Santonian in age.

DISCUSSION

Aeolian and alluvial-fluvial system interaction in intermontane deserts

Wu et al. (2018) and Cao et al. (2020) studied the sedimentary characteristics and internal architecture of aeolian and alluvial-fluvial deposits of the Guifeng Group in the Xinjiang Basin. As an outcome of this work, these researchers identified the intermontane desert environment, although the provenance of the aeolian sediments was not considered. Investigation of the provenance of the aeolian sediments might assist in the interpretation of the interaction between aeolian and alluvial-fluvial sediments in this specific case and for intermontane desert successions more generally.

Climatic deserts are governed dominantly by two competing agents of sediment transport, wind and water (Dickinson and Gehrels, 2009, 2003). Wind-supplied deserts commonly derive sediment from both endogenous and exogenous sources: (i) surrounding bedrock and loose sediment that originally carried by wind or water; and (ii) more distant sediments. Water-supplied deserts commonly derive sediment from (i) exogenous sands that are external but adjacent to the desert system, and (ii) endogenous sands that are entirely within the confines of the desert system (Pastore et al., 2021; Zhu et al., 2014).

For the Xinjiang intermontane desert, the distribution of the detrital zircon U-Pb ages of the sediments of alluvial-fluvial origin is unimodal (i.e., 98–217 Ma), which differs from the multi-modal age distributions of the sediments of aeolian origin (Fig.

7). For the desert-centre setting, the peak of the 1st cluster (i.e., 98–217 Ma) in the aeolian samples is different from that of the alluvial-fluvial samples (Fig. 5). Sedimentary facies analyses by Wu et al. (2018) and Cao et al. (2020) also found no evidence to indicate deposition via aqueous flows in deposits of the desert-centre setting. Thus, available evidence demonstrates that all the sediments from the desert-centre setting are of aeolian origin.

The interaction between fluvial sediment supply and subsequent partial aeolian reworking of that supply is documented at the periphery of several shield-platform deserts (Pastore et al., 2021). In the Xinjiang intermontane desert, the sediments in the desert-margin setting are also a mixture of both wind- and river-transported sediments. The detrital zircons from the desert-margin setting are variably rounded to angular, and have characteristics of transport via both aeolian and alluvial-fluvial processes (Fig. 4). In the Xinjiang intermontane desert, the 1st cluster (98–217 Ma) is the most and least abundant component for the river- and wind-transported sandstones, respectively. For the desert-margin samples, the percentage of the 1st cluster (98–217 Ma) is more abundant than the central-desert samples (Fig. 6). The increase in the proportion of the 1st cluster is influenced by the input of river-transported sediments. In addition, there is one aeolian sandstone sample (JXY-21) from the desert-margin setting that contains more lithics component, which is similar to the alluvial-fluvial samples (Fig. 3).

Based on the above discussion, we propose that the Xinjiang intermontane desert-centre region was entirely controlled by aeolian sedimentary processes, which is similar to much of the present-day Sahara Desert (Pastore et al., 2021). By contrast, the desert margin was controlled by both aeolian and alluvial-fluvial processes, with preserved deposits of both aeolian and alluvial-fluvial facies, similar to parts of the Taklamakan Desert (Rittner et al., 2016). Pastore et al. (2021) suggested that, during the hyperarid episodes, river activity in deserts might be weakened to the extent that the fluvial contribution to and interaction with aeolian dune fields becomes negligible. During the Mid-Late Cretaceous, the intermontane deserts generally developed under hyperarid-arid climates in China (Cao et al., 2020). We, therefore, suggest that aeolian and alluvial-fluvial interactions were likely be confined solely to the marginal areas of this intermontane desert.

Provenance Analysis of the Xinjiang intermontane desert

Source areas of the alluvial-fluvial sandstones

Sandstones of the Hekou and Lianhe formations of alluvial-fluvial origin consist of medium-coarse grained, poorly sorted, and subangular to angular grains, and contain a relatively high content of feldspars and lithic fragments. In addition, their zircon U-Pb ages yield a distinct unimodal distribution (Fig. 5). These observations indicate a relatively proximal source area and a rapid accumulation rate. The palaeocurrent indicators reveal that the sediments were mainly transported from the southeast to the northwest (Fig. 1) (Chen et al., 2016).

These alluvial-fluvial sandstones are dominantly composed of Cretaceous (98–145 Ma) and Jurassic (145–197 Ma) zircons. These zircons are similar to those of the Upper Cretaceous sandstones in the Hengyang Basin (Yan et al., 2011). The Jurassic zircon U-

Pb ages are consistent with the ages of the Yanshanian granites in the SCB (Fig. 7). The Yanshanian magmatism commenced at ca. 190 Ma in the inland region; it propagated from the centre of the SCB and continued in the broad inland region until ca. 150 Ma (Li and Li, 2007). The Cretaceous granitic intrusive rocks (98–145 Ma) in this region occur mainly along the northeast part of the zone between the YB and the CB, and the coastal region (Fig. 7) (Li, 2000). Thus, the nearby SCB and SCMB were the most likely source areas of the alluvial-fluvial sandstones in the Xinjiang intermontane desert.

Source areas of the aeolian sandstones

Sandstones of the Tangbian Formation of aeolian origin are quartz-rich, finer grained and are better sorted and more rounded. They have a wide range of detrital zircon U-Pb ages (Fig. 5). These sediments were likely derived from multiple source areas and underwent long-distant transportation. The most abundant detrital zircon age cluster in the aeolian sandstones is 732–1386 Ma (from Neoproterozoic to Mesoproterozoic). The nearest JNO, a ~970–820 Ma Rodinia margin accretionary belt, is characterized by widely exposed Neoproterozoic basement rocks (Fig. 1). Moreover, ~1550–2000 Ma and ~2300–2600 Ma age populations are common in the JNO (Wang and Zhou, 2012; Li et al., 2018). These three age populations exhibit a perfect match with all the aeolian samples. Therefore, we suggest that the JNO is one of the main sediment sources (Fig. 7).

The detrital zircon age clusters of 98–217 Ma, 220–323 Ma, and 328–482 Ma are closely associated with the Yanshanian, Hercynian-Indosinian, and Caledonian movements, respectively (Li et al., 2014). The Cretaceous (98–145 Ma) and Jurassic

(145–217 Ma) zircons mainly came from Yanshanian granites (80–205 Ma) in the inland region and southeast coast of the SCMB (Li and Li, 2007). The Late Triassic to mid-Carboniferous (220–323 Ma) zircons were mainly derived from Hercynian-Indosinian granites in the failed rift zone between the YB and the CB (Wang et al., 2007). The Devonian to Ordovician (365–482 Ma) zircons also might have been derived from the SCB. Therefore, the SCB and SCMB were likely to also have been major sediment sources (Fig. 7).

A notable age cluster ranges from the Cambrian to Neoproterozoic (503–722 Ma). However, rocks of this age range are generally absent in the SCB, except for the western margin of the SCB (Qi et al., 2023). Moreover, except for contemporaneous (i.e., Late Cretaceous) aeolian deposits in the Jianghan Basin to the west of the Xinjiang Basin (Yu et al., 2020), almost no zircons with this age range had been recognized in the Upper Cretaceous strata in SCB (Li et al., 2017; Hu et al., 2015). Although it accounts for only ca. 5–6% of all the analyzed grains, this age cluster indicates at least one other sediment source area besides JNO, SCB, and SCMB. Although the JNO contains a few zircons of this age range, if zircons of this age in aeolian samples were all from the JNO, the peak age of ~835 Ma would be particularly obvious in the aeolian samples (Fig. 7). However, the aeolian samples do not have the above age signature. As such, even if the JNO contributed zircons of this age, its contribution would be small; the majority of the 500-722 Ma cluster of detrital zircons in the aeolian samples must have been provided by other source areas.

Given the reconstructed ENE direction of the palaeowind (Cao et al., 2020), the sediments might have been derived from west-southwest direction to the Xinjiang Basin (see Appendix S1). The western margin of Yangtze Block (W-YB), which comprises abundant Paleozoic sediments with a peak age of ~558 Ma (Duan et al., 2011), is the most likely source area in the westerly direction (Fig. 7). Another peak age of ~942 Ma of W-YB also appears as a secondary peak in aeolian samples, which further supports the hypothesis that the W-YB is the source area. A minor sediment component from further west could have been derived from the Sanjiang Orogen (SJO) and/or the Songpan-Ganzi terrane (SGT) (Fig. 1), since the detrital zircon ages match for all the potential sources (Enkelmann et al., 2007; Wang et al., 2013). In the north, the age peaks of the South and North Qinling Belt (SQB & NQB) and the southern margin of the North China Block (S-NCB) were not compatible with the ages indicated by our aeolian samples (Li et al., 2018). In addition, compared with other detrital zircons in the aeolian samples, the forms of zircons with the age of 503–722 Ma tend to be relatively complete and more angular. These observations may indicate that the aeolian sand originating from the W-YB source was transported as a suspended load to the Xinjiang Basin by the dominant westerlies (Fig. 4 and Fig. S4). Moreover, along the pathway from the W-YB to the Xinjing Basin, the zircons with this age range were also identified in contemporaneous aeolian deposits in the Jianghan Basin (Fig. 8), which represents secondary peaks with similar contents as the Tangbian Formation in the Xinjiang intermontane desert (Li et al., 2018b; Yu et al., 2020).

In summary, the aeolian sandstones in the Xinjiang intermontane desert were derived from multiple sources. The JNO, SCB, and SCMB were the main sources; the

W-YB was an important secondary source; and the even more distant SJO and SGT were other potential sources.

Ultra-long-Distance Transport of Aeolian Sand

A secondary but significant source area of the sediments in the Xinjiang intermontane desert was the western margin of Yangtze Block (W-YB), which was more than a thousand kilometres away from the Xinjiang Basin. In the Xinjiang Basin, the diameters of the detrital zircons within the relevant age cluster (503–722 Ma) are close to or over 100 μm (Fig. S4). Therefore, our results suggest that sand with a diameter of over 100 μm could be transported over one thousand kilometres by a dominant westerly wind from western China to southeastern China (Fig. 8).

It has been shown that fine silt (2-20 μm) can be transported over thousands of kilometres and coarse silt (21-63 μm) can be transported over hundreds of kilometres by winds (Lancaster, 2020). However, previous studies have suggested that very-fine sand (63-125 μm) could only be transported within a few kilometres in short-term suspension or modified saltation by the wind (Tsoar and Pye, 1987; Lancaster, 2020). Hence, the ultra-long-distance aeolian transport of sand grains with a diameter over 100 μm requires a wind with a sustained high speed and a favourable geographic arrangement.

The equation in Tsoar and Pye (1987) provides important constraints on the relationships of transport distance, wind speed, and particle size for aeolian grains in suspension.

$$L = \bar{U}2\varepsilon/K^2D^4$$

where L is transport distance, $\bar{U}$ is mean wind speed, ε is the coefficient of turbulent exchange, $K = \rho_s g/18\mu$ (where ρ_s is the grain density; μ is the dynamic velocity of air; g is gravity), and D is the grain diameter (Tsoar and Pye, 1987). Based on this equation, to transport quartz spheres with a diameter of ~100 μm for 1000 km, the minimum wind speed is 24 m/s (i.e., a strong gale).

We also evaluate the possibility that the aeolian sediments were transported intermittently along the 1000 km-long sediment transport pathway. For such intermittent sediment transport, the intermittently deposited sediments would likely have been prone to reworking by fluvial erosional processes, and the zircons within the relevant age cluster (503–722 Ma) would be expected to be present along the pathway from the W-YB to the Xinjiang Basin in a decreasing amount. However, there is no other known record of 503–722 Ma zircons along the path from the W-YB to the Xinjing Basin, except for contemporaneous aeolian deposits in the Jianghan Basin, which also show secondary peaks and similar contents as the Tangbian Formation in the Xinjiang intermontane desert (Li et al., 2018b; Yu et al., 2020). This suggests that the ultra-long-distance aeolian sediment transport could have occurred entirely in suspension as a single event.

Currently, the annual mean surface westerly wind speed ranges from only 1 m/s to 9 m/s, although the transient speed of the westerly jet can be considerably higher, e.g., 182.5 m/s in the polar front of the jet stream (Schiemann et al., 2009). Neither the low annual mean wind speed nor the strong transient wind speed in tropopause would have been sufficient to transport the ~100 μm sand grains over 1000 km. Based on the Late Cretaceous global climate modelling results (Floegel and Wagner, 2006), strong westerlies typically lie between the subtropical highs at 30°. Based on these modelling results, the surface westerlies were considerably stronger in the northern than in the southern hemisphere, with wind speeds up to 11 m/s. This would have strengthened the transportation of ~100 μm sand at high altitudes. In addition, Koopmann (1981) argued that the atmospheric circulation and planetary winds were heightened during episodes of dry glacial climate conditions, and that aeolian sand transport would be enhanced during such episodes. For example, the coarse sand grains from the Sahara Desert were transported to the Atlantic Ocean by winds during the Late Cenozoic glacial periods (Koopmann, 1981). The early Late Cretaceous was one of the warmest periods of the Phanerozoic, but the temperature tended to decrease gradually from Turonian to Santonian (Bornemann et al., 2008; O'Brien et al., 2017). According to a compilation of dropstones, tillites, glendonites, eustasy fluctuations, and $\delta^{18}O$ values, five glacial events during the Mid-Late Cretaceous were recognized in the Albian-Cenomanian boundary, middle and latest Cenomanian, middle Turonian, middle Coniacian, and early Santonian (Bornemann et al., 2008; Chen, 2011; Ladant and Donnadieu, 2016). However, the chronological relationship between the aeolian sandstones in Xinjiang Basin and the Cretaceous glacial events is not rigidly constrained. In addition, the occurrences of striated cobbles in the alluvial facies close to the Xinjiang palaeo-intermontane desert may suggest glacial activity (Jiao et al., 2020). We propose that temporary glacial events might have acted as a trigger for westerlies burst with heightened gale-force wind events capable of transporting sand over an ultra-long distance. And a sustained heightening of wind speed would lead to a relatively high proportion of sand derived from the W-YB being carried to the Xinjiang intermontane desert. In this study, since the aeolian sediments from the W-YB only account for ~6% of the total, we speculate that the westerlies were only intermittently strengthened during the Mid-Late Cretaceous.

Compared to silts (dusts) that are carried at high altitudes in suspension, sands are usually carried at lower altitudes and are easily blocked by highlands and mountains. Du et al. (2018) demonstrated that the far-traveled input from the Tarim Basin to the Qaidam Desert is transported through the low areas among the Altyn Tagh Mountains at present in northwestern China. Therefore, a low-relief corridor conducive to aeolian sand transport is also a prerequisite for the ultra-long-distance transportation. According to the Mid-Late Cretaceous palaeogeographic map (Ma et al., 2009; Wang, 1985), there was a relatively low-elevation and low-relief corridor between the Southwest China Highland and Palaeo-Qinling-Dabie Mountains. This corridor may have served as a pathway for the ultra-long-distance sand transport from the W-YB to southeastern China (Fig. 8).

CONCLUSIONS AND IMPLICATIONS

The results of this study suggest that sand of the Cretaceous Xinjiang intermontane desert was dominantly supplied by aeolian processes, although the desert margin region also received subordinate river-transported sediments. Based on the sandstone petrography, detrital zircon morphology, and U-Pb geochronology, the nearby South China Craton (SCB) and South China Magmatic Belt (SCMB) were the main sediment sources for the Xinjiang intermontane desert. Importantly, the western margin of the Yangtze Block (W-YB) was a notable secondary sediment source; this demonstrates an ultra-long aeolian sand transport pathway of more than 1000 km to the Xinjiang intermontane desert. During the Late Cretaceous, the westerlies were stronger in the northern than in the southern hemisphere, with approximately doubled wind speeds. In such a climatic context, we suggest that the ultra-long aeolian sediment transport was further facilitated by a combination of both (i) the intermittently strengthened westerly winds during short-lived glacial episodes and (ii) the presence of a low-elevation, low-relief corridor that served as a sediment transport route from source to sink across southern China.

The results presented herein study also have implications for the development of intermontane deserts more generally. This study demonstrates a plausible relationship between the intermontane deserts and greenhouse climate state. Elevated levels of global atmospheric CO_2 concentration increase the likelihood of development of intermontane deserts during the greenhouse periods. Such conditions might arise in the near future. To further constrain the above issue, more work is needed to investigate the formative mechanisms and the climatic affinities of intermontane deserts in deep time. In addition, previous studies have demonstrated how rainshadow effects caused by the East Asian coastal mountains may have acted to facilitate the development of the Mid-Late Cretaceous intermontane deserts in South China. Nowadays, there are many sand dunes constructed in intermontane basins that border high mountain ranges, notablythe Himalaya and Andes. We propose that these sand-dune fields that are currently of modest extent in rainshadow-affected intermontane basins may evolve into larger intermontane deserts in the near future. Additional study, including both monitoring of modern systems and deep-time investigations of successions preserved in the rock record are required.

ACKNOWLEDGEMENTS

The authors are grateful to the Editor Dr. Alexander Brasier and Dr. Gonzalo Veiga，and thank Dr. Chihua Wu and two anonymous reviewers for their helpful comments and suggestions on the earlier versions of this manuscript. The authors also thank Rong Chai for discussion. This study was financially supported by the National Natural Science Foundation of China (grants 41888101, 42072116, 42102122, 41790455), the National Key R&D Plan of China (Grant 2018YFE0204204), and the Chinese "111" project (Grant B20011).

REFERENCES CITED

Andersen, T. (2002) Correction of common lead in U–Pb analyses that do not report 204Pb. *Chemical Geology*, **192,** 59-79.

Barbolini, N., Woutersen, A., Dupont-Nivet, G., Silvestro, D., Tardif, D., Coster, P.M.C., Meijer, N., Chang, C., Zhang, H.X., Licht, A., Rydin, C., Koutsodendris, A., Han, F., Rohrmann, A., Liu, X.-J., Zhang, Y., Donnadieu, Y., Fluteau, F.,

Ladant, J.-B., Hir, G.L. and Hoorn, C. (2020) Cenozoic evolution of the steppe-desert biome in Central Asia. *Science Advances*, **6,** eabb8227.

Bertolini, G., Marques, J.C., Hartley, A.J., Da-Rosa, A.A.S., Scherer, C.M.S., Basei, M.A.S. and Frantz, J.C. (2020) Controls on Early Cretaceous desert sediment provenance in south-west Gondwana, Botucatu Formation (Brazil and Uruguay). *Sedimentology*, **67,** 2672-2690.

Bornemann, A., Norris, R.D., Friedrich, O., Beckmann, B., Schouten, S., Damsté, J.S.S., Vogel, J., Hofmann, P. and Wagner, T. (2008) Isotopic Evidence for Glaciation During the Cretaceous Supergreenhouse. *Science*, **319**, 189-192.

Brookfield, M.E. (1980) Permian intermontane basin sedimentation in southern Scotland. *Sedimentary Geology*, **27**, 167-194.

Brookfield, M. and Silvestro, S. (2010) Eolian Systems. In: *Facies Models* (Eds R.W. Dalrymple and N.P. James) 4 edn. Geological Association of Canada, St. John's, Nfld.

Cao, S., Zhang, L., Wang, C., Ma, J., Tan, J. and Zhang, Z. (2020) Sedimentological characteristics and aeolian architecture of a plausible intermountain erg system in Southeast China during the Late Cretaceous. *GSA Bulletin*, **132,** 2475-2488.

Caesar, J., Palin, E., Liddicoat, S., Lowe, J., Burke, E., Pardaens, A., Sanderson, M. and Kahana, R. (2013) Response of the HadGEM2 Earth System Model to Future Greenhouse Gas Emissions Pathways to the Year 2300. *Journal of Climate*, **26**, 3275-3284.

Cawood, P.A., Zhao, G., Yao, J., Wang, W., Xu, Y. and Wang, Y. (2018) Reconstructing South China in Phanerozoic and Precambrian supercontinents. *Earth-*

Science Reviews, **186,** 173-194.

Chen, L., Guo, F., Steel, R.J. and Li, Y. (2016) Petrography and geochemistry of the Late Cretaceous redbeds in the Gan-Hang Belt, southeast China: implications for provenance, source weathering, and tectonic setting. *International Geology Review*, **58,** 1196-1214.

Chen, L., Steel, R.J., Guo, F., Olariu, C. and Gong, C. (2017) Alluvial fan facies of the Yongchong Basin: Implications for tectonic and paleoclimatic changes during Late Cretaceous in SE China. *Journal of Asian Earth Sciences*, **134,** 37-54.

Chen, Q., Pang, F. and Qu, D. (2008) Depositional and reservoir characteristics of the Cretaceous Chishan Formation in Subei Basin and their significance. *Marine and Petroleum Geology*, **28**, 95-100.

Chen, X., Wang, C. and H, Y. (2011) Progress in the study of Cretaceous rapid climate change: evidence of glaciation in a greenhouse world. *Geoscience*, **25**, 409-418.

Cooke, R.U., Warren, A. and Goudie, A.S. (1993) *Desert geomorphology*. CRC Press.

Dickinson, W.R. (1985) Interpreting Provenance Relations from Detrital Modes of Sandstones. In: *Provenance of Arenites* (Ed G.G. Zuffa), pp. 333-361. Springer Netherlands, Dordrecht.

Dickinson, W.R. and Gehrels, G.E. (2003) U–Pb ages of detrital zircons from Permian and Jurassic eolian sandstones of the Colorado Plateau, USA: paleogeographic implications. *Sedimentary Geology*, **163,** 29-66.

Dickinson, W.R. and Gehrels, G.E. (2009) U-Pb ages of detrital zircons in Jurassic eolian and associated sandstones of the Colorado Plateau: Evidence for transcontinental dispersal and intraregional recycling of sediment. *GSA Bulletin*, **121,** 408-433.

Du, S., Wu, Y. and Tan, L. (2018) Geochemical evidence for the provenance of aeolian deposits in the Qaidam Basin, Tibetan Plateau. *Aeolian Research*, **32,** 60-70.

Du, X., Chen, X., Wang, C., Wei, Y., Li, Y. and Jansa, L. (2015) Geochemistry and detrital zircon U–Pb dating of Lower Cretaceous volcaniclastics in the Babazhadong section, Northern Tethyan Himalaya: Implications for the breakup of Eastern Gondwana. *Cretaceous Research*, **52,** 127-137.

Duan, L., Meng, Q. R., Zhang, C. L. and Liu, X. M. (2011) Tracing the position of the South China block in Gondwana: U–Pb ages and Hf isotopes of Devonian detrital zircons. *Gondwana Research*, **19,** 141-149.

Enkelmann, E., Weislogel, A., Ratschbacher, L., Eide, E., Renno, A. and Wooden, J. (2007) How was the Triassic Songpan-Ganzi basin filled? A provenance study. *Tectonics*, **26**, TC4007.

Floegel, S. and Wagner, T. (2006) Insolation-control on the Late Cretaceous hydrological cycle and tropical African climate—global climate modelling linked to marine climate records. *Palaeogeography, Palaeoclimatology, Palaeoecology*, **235**, 288-304.

Garzanti, E. (2019) Petrographic classification of sand and sandstone. *Earth-Science Reviews*, **192,** 545-563.

Garzanti, E., Vermeesch, P., Andò, S., Lustrino, M., Padoan, M. and Vezzoli, G. (2014) Ultra-long distance littoral transport of Orange sand and provenance of the Skeleton Coast Erg (Namibia). *Marine Geology*, **357,** 25-36.

Gehrels, G. (2012) Detrital Zircon U-Pb Geochronology: Current Methods and New Opportunities. In: *Tectonics of Sedimentary Basins* (Eds Busby, C.J. and Azor, A.), John Wiley & Sons, Ltd, Chichester, UK, pp. 45-62.

Guo, F., Zhu, Z., Huang, B. and Jiang, Y. (2013) Cretaceous sedimentary system and their relationship with Danxia landform in Xinjiang Basin, Jiangxi. *Acta Sedimentologica Sinica*, **31,** 954-964.

Hasegawa, H., Tada, R., Jiang, X., Suganuma, Y., Imsamut, S., Charusiri, P., Ichinnorov, N. and Khand, Y. (2012) Drastic shrinking of the Hadley circulation during the mid-Cretaceous Supergreenhouse. *Climate of the Past*, **8,** 1323-1337.

Hu, L., Cawood, P.A., Du, Y., Yang, J. and Jiao, L. (2015) Late Paleozoic to Early Mesozoic provenance record of Paleo-Pacific subduction beneath south China. *Tectonics*, **34,** 986-1008.

Ingersoll, R.V., Bullard, T.F., Ford, R.L., Grimm, J.P., Pickle, J.D. and Sares, S.W. (1984) The effect of grain size on detrital modes: a test of the Gazzi-Dickinson point-counting method. *Journal of Sedimentary Research*, **54,** 103-116.

Intergovernmental Panel on Climate, C. (2014) *Climate Change 2014 – Impacts, Adaptation and Vulnerability: Part A: Global and Sectoral Aspects: Working Group II Contribution to the IPCC Fifth Assessment Report: Volume 1: Global and Sectoral Aspects*. Cambridge University Press, Cambridge.

Jiang, Q. and Yang, X. (2019) Sedimentological and Geochemical Composition of Aeolian Sediments in the Taklamakan Desert: Implications for Provenance and Sediment Supply Mechanisms. *Journal of Geophysical Research: Earth Surface*, **124**, 1217-1237.

Jian, X., Weislogel, A. and Pullen, A. (2019) Triassic Sedimentary Filling and Closure of the Eastern Paleo-Tethys Ocean: New Insights From Detrital Zircon Geochronology of Songpan-Ganzi, Yidun, and West Qinling Flysch in Eastern Tibet. *Tectonics*, **38**, 767-787.

Jiang, X., Pan, Z. and Fu, Q. (1999) The variations of palaeowind direction of the Cretaceous desert in the Sichuan Basin and their significance. S*edimentary Facies and Palaeogeography*, **1**, 3-13.

Jiang, X., Pan, Z., Xu, J., Li, X., Xie, G. and Xiao, Z. (2008) Late Cretaceous aeolian dunes and reconstruction of palaeo-wind belts of the Xinjiang Basin, Jiangxi Province, China. *Palaeogeography, Palaeoclimatology, Palaeoecology*, **257,** 58-66.

Jiao, H., Wu, C., Rodríguez-López, J.P., Sun, X. and Yi, H. (2020) Late Cretaceous plateau deserts in the South China Block, and Quaternary analogues; sedimentology, dune reconstruction and wind-water interactions. *Marine and Petroleum Geology*, **120,** 104504.

Kinny, P.D., Wijbrans, J.R., Froude, D.O., Williams, I.S. and Compston, W. (1990) Age constraints on the geological evolution of the Narryer Gneiss Complex, Western Australia. *Australian Journal of Earth Sciences*, **37,** 51-69.

Kocurek, G. and Lancaster, N. (1999) Aeolian system sediment state: theory and Mojave Desert Kelso dune field example. *Sedimentology*, **46**, 505-515.

Koopmann, B. (1981) Sedimentation von Saharastaub im subtropischen Nordatlantik während der letzten 25.000 Jahre. *"Meteor" Forschungs-Ergebnisse, C*, **35,** 23-59.

Ladant, J. B. and Donnadieu, Y. (2016) Palaeogeographic regulation of glacial events during the Cretaceous supergreenhouse. *Nature Communications*, **7,** 12771.

Lancaster, N. (2020) On the formation of desert loess. *Quaternary Research*, **96,** 105-122.

Lancaster, N., Yang, X. and Thomas, D. (2013) Spatial and temporal complexity in Quaternary desert datasets: implications for interpreting past dryland dynamics and understanding potential future changes. *Quaternary Science Reviews*, **78,** 301-302.

Li, J., Zhang, Y., Dong, S. and Johnston, S.T. (2014) Cretaceous tectonic evolution of South China: A preliminary synthesis. *Earth-Science Reviews*, **134,** 98-136.

Li, J., Zhang, Y., Zhao, G., Johnston, S.T., Dong, S., Koppers, A., Miggins, D.P., Sun, H., Wang, W. and Xin, Y. (2017) New insights into Phanerozoic tectonics of South China: Early Paleozoic sinistral and Triassic dextral transpression in the east Wuyishan and Chencai domains, NE Cathaysia. *Tectonics*, **36,** 819-853.

Li, X. H. (2000) Cretaceous magmatism and lithospheric extension in Southeast China. *Journal of Asian Earth Sciences*, **18,** 293-305.

Li, G., Wu, C., Rodríguez-López, J.P., Yi, H., Xia, G. and Wagreich, M. (2018a) Mid-Cretaceous aeolian desert systems in the Yunlong area of the Lanping Basin, China: Implications for palaeoatmosphere dynamics and paleoclimatic change in East Asia. *Sedimentary Geology*, **364**, 121-140.

Li, Y., He, D., Li, D., Lu, R., Fan, C., Sun, Y. and Huang, H. (2018b) Sedimentary provenance constraints on the Jurassic to Cretaceous paleogeography of Sichuan Basin, SW China. *Gondwana Research*, **60,** 15-33.

Li, Z. X. and Li, X. H. (2007) Formation of the 1300-km-wide intracontinental orogen and postorogenic magmatic province in Mesozoic South China: A flat-slab subduction model. *Geology*, **35,** 179-182.

Lindholm, R. (2012) *A practical approach to sedimentology*. Springer Science & Business Media.

Ludwig, K.R. (2003) User's manual for isoplot 3.00, a geochronlogical toolkit for microsoft excel. *Berkeley Geochronl. Cent. Spec. Publ.*, **4,** 25-32.

Lugli, S., Dori, S.M. and Fontana, D. (2007) Alluvial sand composition as a tool to unravel late Quaternary sedimentation of the Modena Plain, northern Italy. In: *Sedimentary Provenance and Petrogenesis: Perspectives from Petrography and Geochemistry* (Eds Arribas, J., Critelli, S., Johnsson, M. J.), Geol. Soc. Am. Sp. Paper, **420**, 57-72.

Ma, Y., Chen, H. and Wang, G. (2009) Sequence stratigraphy and paleogeography in South China. *Science Press, Beijing*.

Maas, R., Kinny, P.D., Williams, I.S., Froude, D.O. and Compston, W. (1992) The Earth's oldest known crust: A geochronological and geochemical study of 3900–4200 Ma old detrital zircons from Mt. Narryer and Jack Hills, Western Australia. *Geochimica et Cosmochimica Acta*, **56,** 1281-1300.

Mountney, N.P. (2006) Eolian facies models. In: *Facies Models Revisited* (Ed R.G.W. H.W. Posamentier), **Special Publication**, pp. 19-83. Society for Economic Paleontologists and Mineralogists, Tulsa, Oklahoma.

Mu, H., Yan, D.-P., Qiu, L., Yang, W.-X., Kong, R.-Y., Gong, L.-X. and Li, S. (2019)

Formation of the Late Triassic western Sichuan foreland basin of the Qinling Orogenic Belt, SW China: Sedimentary and geochronological constraints from the Xujiahe Formation. *Journal of Asian Earth Sciences*, **183**, 103938.

Muhs, D.R. (2004) Mineralogical maturity in dunefields of North America, Africa and Australia. *Geomorphology*, **59,** 247-269.

Muhs, D.R., Lancaster, N. and Skipp, G.L. (2017) A complex origin for the Kelso Dunes, Mojave National Preserve, California, USA: A case study using a simple geochemical method with global applications. *Geomorphology*, **276**, 222-243.

O'Brien, C.L., Robinson, S.A., Pancost, R.D., Sinninghe Damsté, J.S., Schouten, S., Lunt, D.J., Alsenz, H., Bornemann, A., Bottini, C., Brassell, S.C., Farnsworth, A., Forster, A., Huber, B.T., Inglis, G.N., Jenkyns, H.C., Linnert, C., Littler, K., Markwick, P., McAnena, A., Mutterlose, J., Naafs, B.D.A., Püttmann, W., Sluijs, A., van Helmond, N.A.G.M., Vellekoop, J., Wagner, T. and Wrobel, N.E. (2017) Cretaceous sea-surface temperature evolution: Constraints from TEX86 and planktonic foraminiferal oxygen isotopes. *Earth-Science Reviews*, **172**, 224-247.

Pastore, G., Baird, T., Vermeesch, P., Bristow, C., Resentini, A. and Garzanti, E. (2021) Provenance and recycling of Sahara Desert sand. *Earth-Science Reviews*, **216,** 103606.

Qi, L., Hou, M., Cawood, P.A., Lang, X., Zhu, S. and Zhang, M. (2023) Neoproterozoic storm deposits in western Yangtze: Implications for the sea conditions during the middle Sturtian glaciation. *Precambrian Research*, **384**, 106945.

Rittner, M., Vermeesch, P., Carter, A., Bird, A., Stevens, T., Garzanti, E., Andò, S.,

Vezzoli, G., Dutt, R., Xu, Z. and Lu, H. (2016) The provenance of Taklamakan desert sand. *Earth and Planetary Science Letters*, **437,** 127-137.

Rodríguez-López, J.P., Clemmensen, L.B., Lancaster, N., Mountney, N.P. and Veiga, G.D. (2014) Archean to Recent aeolian sand systems and their sedimentary record: Current understanding and future prospects. *Sedimentology*, **61,** 1487-1534.

Schiemann, R., Lüthi, D. and Schär, C. (2009) Seasonality and interannual variability of the westerly jet in the Tibetan Plateau region. *Journal of Climate*, **22,** 2940-2957.

Shen, C., Donelick, R.A., O'Sullivan, P.B., Jonckheere, R., Yang, Z., She, Z., Miu, X. and Ge, X. (2012) Provenance and hinterland exhumation from LA-ICP-MS zircon U–Pb and fission-track double dating of Cretaceous sediments in the Jianghan Basin, Yangtze block, central China. *Sedimentary Geology*, 281, 194-207.

Shu, L.S., Zhou, X.M., Deng, P., Wang, B., Jiang, S.Y., Yu, J.H. and Zhao, X.X. (2009) Mesozoic tectonic evolution of the Southeast China Block: New insights from basin analysis. *Journal of Asian Earth Sciences*, **34,** 376-391.

Tsoar, H. and Pye, K. (1987) Dust transport and the question of desert loess formation. *Sedimentology*, **34,** 139-153.

Walker, J.D., Martin, M.W., Glazner, A.F. and Bartley, J.M. (2002) Late Paleozoic to Mesozoic development of the Mojave Desert and environs, California. In: *Geologic Evolution of the Mojave Desert and Southwestern Basin and Range* (Eds Glazner A.F., Walker J.D., Bartley J.M.), Geological Society of America Memoir, **195**, 1-18.

Wang, B. Q., Wang, W., Chen, W.T., Gao, J. F., Zhao, X. F., Yan, D. P. and Zhou, M. F. (2013) Constraints of detrital zircon U–Pb ages and Hf isotopes on the provenance of the Triassic Yidun Group and tectonic evolution of the Yidun Terrane, Eastern Tibet. *Sedimentary Geology*, **289,** 74-98.

Wang, D. and Shu, L. (2012) Late Mesozoic basin and range tectonics and related magmatism in Southeast China. *Geoscience Frontiers*, **3,** 109-124.

Wang, W. and Zhou, M.-F. (2012) Sedimentary records of the Yangtze Block (South China) and their correlation with equivalent Neoproterozoic sequences on adjacent continents. *Sedimentary Geology*, **265-266,** 126-142.

Wang, Y., Fan, W., Zhao, G., Ji, S. and Peng, T. (2007) Zircon U–Pb geochronology of gneissic rocks in the Yunkai massif and its implications on the Caledonian event in the South China Block. *Gondwana Research*, **12,** 404-416.

Whitford, W.G. and Duval, B.D. (2019) *Ecology of desert systems*. Academic Press.

Williams, M. (2015) Interactions between fluvial and eolian geomorphic systems and processes: Examples from the Sahara and Australia. *CATENA*, **134**, 4-13.

Wu, C., Liu, C., Haisheng, Y., Xia, G., Zhang, H., Wang, L., Li, G. and Wagreich, M. (2017) Mid-Cretaceous desert system in the Simao Basin, southwestern China, and its implications for sea-level change during a greenhouse climate. *Palaeogeography, Palaeoclimatology, Palaeoecology*, **468,** 529-544.

Wu, C., Rodríguez-López, J.P., Liu, C., Sun, X., Wang, J., Xia, G. and Wagreich, M. (2018a) Late Cretaceous climbing erg systems in western Xinjiang Basin. Palaeoatmosphere dynamics and East Asia margin tectonic forcing on desert expansion and preservation. *Marine and Petroleum Geology*, **93,** 539-552.

Wu, H., Zhang, L., Gao, J., Zhang, M., Zhu, M. and Xiang, P. (2018b) U–Pb geochronology, isotope systematics, and geochemical characteristics of the Triassic Dasuji porphyry Mo deposit, Inner Mongolia, North China: Implications for tectonic evolution and constraints on the origin of ore-related granitoids. *Journal of Asian Earth Sciences*, **165,** 132-144.

Xi, D., Wan, X., Li, G. and Li, G. (2019) Cretaceous integrative stratigraphy and timescale of China. *Science China Earth Sciences*, **62,** 256-286.

Yan, Y., Hu, X.-q., Lin, G., Santosh, M. and Chan, L.-S. (2011) Sedimentary provenance of the Hengyang and Mayang basins, SE China, and implications for the Mesozoic topographic change in South China Craton: Evidence from detrital zircon geochronology. *Journal of Asian Earth Sciences*, **41,** 494-503.

Yu, X., Liu, C., Wang, C., Li, F. and Wang, J. (2020) Eolian deposits of the northern margin of the South China (Jianghan Basin): Reconstruction of the Late Cretaceous East Asian landscape in central China. *Marine and Petroleum Geology*, **117**, 104390.

Yu, X., Liu, C., Wang, C. and Wang, J. (2021a) Late Cretaceous aeolian desert system within the Mesozoic fold belt of South China: Palaeoclimatic changes and tectonic forcing of East Asian erg development and preservation. *Palaeogeography, Palaeoclimatology, Palaeoecology*, **567**, 110299.

Yu, X., Wang, C., Bertolini, G., Liu, C. and Wang, J. (2021b) Damp- to dry aeolian systems: Sedimentology, climate forcing, and aeolian accumulation in the Late Cretaceous Liyou Basin, South China. *Sedimentary Geology*, **426**, 106030.

Zhang, C., Li, Z., Chen, Q., Dong, S., Yu, X. and Yu, Q. (2020) Provenance of eolian sands in the Ulan Buh Desert, northwestern China, revealed by heavy mineral assemblages. *CATENA*, **193,** 104624.

Zhu, B., Yu, J., Qin, X., Rioual, P., Liu, Z. and Xiong, H. (2014) Formation and evolution of sand deserts in Xinjiang, Northwest China: I. Provenances of desert sands. *Journal of Geographical Sciences*, **24,** 177-190.

FIGURE CAPTIONS

Fig. 1. (A) Sketch map showing the location of South China, modified after Li et al. (2017). (B) Simplified geological map of South China delineating the distributions of the Archean-Cretaceous strata and igneous rocks. Modified after Li et al. (2017). (C) Geological and palaeogeographic map of the Xinjiang Basin. Blue circles represent sampling sites and black-rimmed circles represent detrital zircon samples.

Fig. 2. The Cretaceous strata in the Xinjiang Basin. In the fourth column, according to Li et al. (2019), the Hekou, Tangbian, and Lianhe formations were deposited coevally. The Hekou and Lianhe formations represent the same lithostratigraphic unit in different geographic locations. These formations predominately comprise gravel facies of flood origin accumulated at the foot of mountains in the southern and northern margins of the Xinjiang Basin. Basinwards, these alluvial facies gradually transition to aeolian facies of the Tangbian Formation. Fm. = Formation and Gr. = Group.

Fig. 3. Thin-section photo-micrography of (A) alluvial sediments, (B) fluvial sediments, (C) aeolian sediments from the desert-centre setting, and (D) aeolian sediments from the desert-margin setting. (E) Q-F-L ternary diagram based on Garzanti et al. (2019). Q = quartzose, Qs = single-crystal quartz, Qp = polycrystal quartz, F = feldspathic, L = lithic, Ls = sedimentary lithics, lFQ = litho-feldspatho-quartzose, lQF = litho-quartzo-feldspathic, qLF = quartzo-lithofeldspathic, qFL = quartzo-feldspatho-lithic, fQL = feldspatho-quartzo-lithic, and fLQ = feldspatho-litho-quartzose.

Fig. 4. Cathodoluminescence (CL) images of representative zircon grains from the Xinjiang intermountain desert. The small white circles show the sites for U–Pb age analyses and the ages (Ma). YT-03 & YT-08 were taken from aeolian sediments in the desert-centre setting; YT-07 & YT-13 were taken from aeolian sediments in the desert-margin setting; YT-12 & YT-14 were taken from the alluvial-fluvial sediments.

Fig. 5. U–Pb concordia diagrams and normalized probability density distributions (blue curves).

Fig. 6. Bar graph shows percentages of age populations (Ma) for each sample.

Fig. 7. Zircon U–Pb age probability density plots of the Mid-Late Cretaceous sediments in the Xinjiang intermountain desert and potential source regions. All zircon ages show discordance <10%. The zircon ages are divided into seven population groups: 98-217

Ma, 220-323 Ma, 328-482 Ma, 503-722 Ma, 732–1386 Ma, 1426-2174 Ma, and 2210-2701 Ma. JNO—Jiangnan Orogen, YB-Yangtze Block, CB—Cathaysia Block, SCMB—South China Magmatic Belt, W-YB—Western margin of Yangtze Block, SJO—Sanjiang Orogen, SGT—Songpan-Ganzi terrane, NQB—North Qinling Belt, SQB—South Qinling Belt, and S-NCB—Southern margin of the North China Block. Data: JNO, W-YB, SJO, SGT, NQB, SQB, S-NCB derived from Li et al. (2018), YB derived from Jian et al. (2019), CB derived from Mu et al. (2019), and SCMB derived from Yan et al. (2011).

Fig. 8. Palaeogeographic map of southern China during the Mid-Late Cretaceous. Modified after Wang (1985) and Ma et al. (2009). The mid-Cretaceous intermontane desert in the Xinjiang Basin was mainly controlled by westerlies (green arrows). The reconstructed palaeowind direction was toward the ENE. Since the South China Block rotated by 16.7 ± 5.0° during mid-Cretaceous to Paleogene, so the palaeowind direction depicted on the modern map is nearly directly eastward. SC—Sichuan Basin, JB—Jianghan Basin, CL—Chaling Basin, XJ—Xinjiang Basin, and SB—Subei Basin.

TABLE CAPTIONS

Table 1. Maximum depositional ages calculated from zircon U-Pb geochronology of sandstone samples from the Xinjiang Basin

SUPPORTING INFORMATION

S1. Reconstruction of palaeowind directions for the Late Cretaceous Xinjiang intermontane desert.

Fig. S1. Outcrops and line drawings of (A) small-scale barchan dunes, (B) large-scale compound transverse dunes and (C) large-scale complex dunes. Black lines represent aeolian surfaces (interdune migration surfaces, superimposition surfaces, and reactivation surfaces); and gray, dashed lines represent cross-stratification. The numbers before each arrow/after each arrow represent the azimuth/dip of the cross beddings. Modified from Cao et al., 2020.

Fig. S2. Palaeogeographic map and palaeowind directions of the Tangbian Formation in the Xinjiang Basin during the Late Cretaceous. Modified from Cao et al., 2020.

Fig. S3. Crossplot of Th/U ratios versus U–Pb ages of concordant detrital zircons from sandstones in the Xinjiang intermontane desert.

Fig. S4. Cathodoluminescence (CL) images of representative 503-722 Ma zircon grains from the Xinjiang intermontane desert. The small white circles show the sites for U–Pb age analyses and the ages (Ma). YT-08 was taken from aeolian sediments in the desert center, and YT-07 & YT-13 were taken from aeolian sediments in the desert margin.

Table S1. Location information of 14 sandstone samples throughout the Xinjiang Basin.

Table S2. Laser ablation inductively coupled plasma spectrometry (LA-ICP-MS) data of detrital zircons from the Xinjiang intermontane desert in SE China.

Figure 1

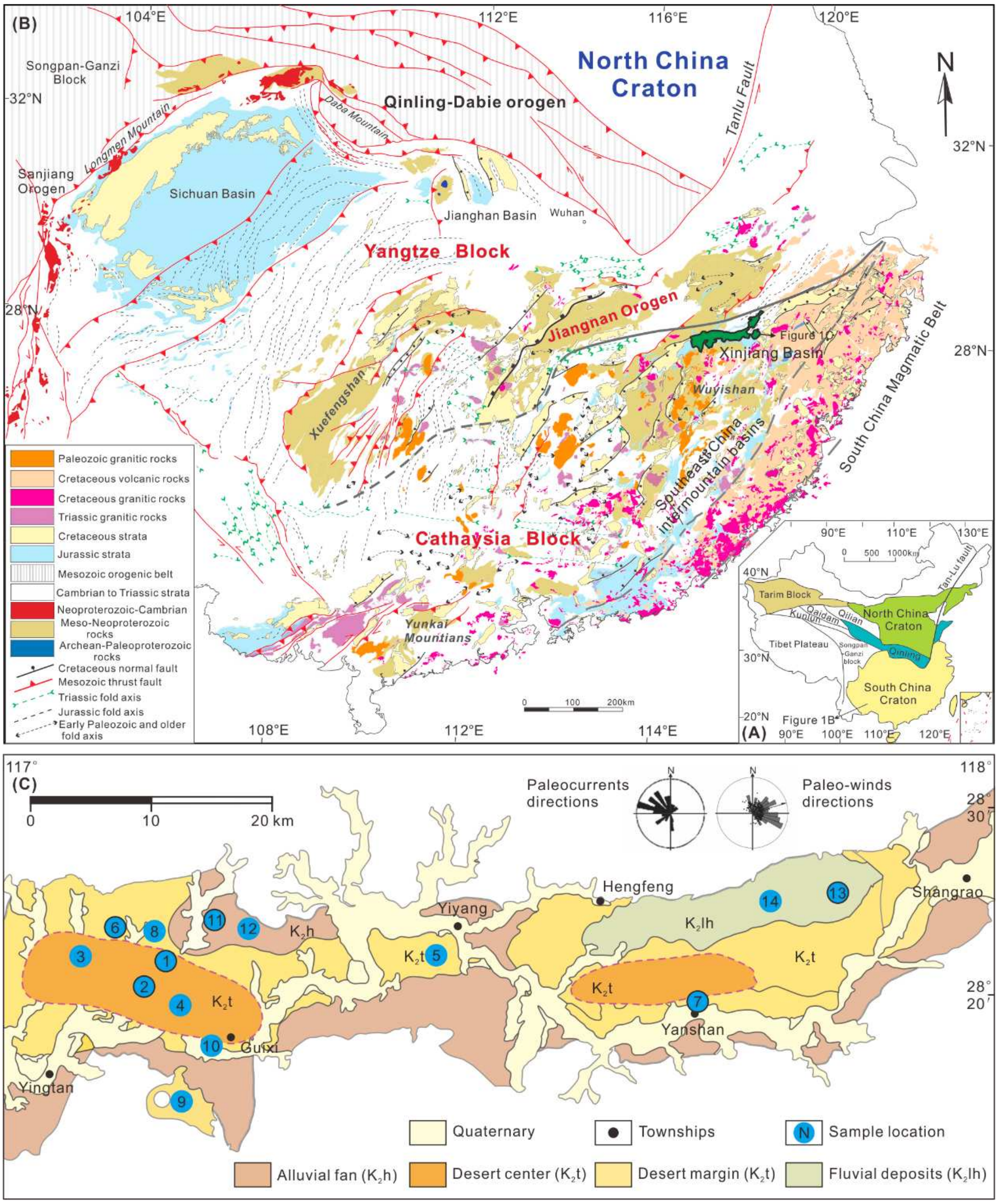

(B)
104°E
112°E
116°E
120°E
North China Craton
Songpan-Ganzi Block
32°N
Qinling-Dabie orogen
Longmen Mountain
Daba Mountain
Tanlu Fault
Sanjiang Orogen
Sichuan Basin
Jianghan Basin
Wuhan
Yangtze Block
28°N
Jiangnan Orogen
Figure 1C
Xinjiang Basin
Xuefengshan
Wuyishan
South China Magmatic Belt
Southeast China intermountain basins
Cathaysia Block
Yunkai Mountians
Paleozoic granitic rocks
Cretaceous volcanic rocks
Cretaceous granitic rocks
Triassic granitic rocks
Cretaceous strata
Jurassic strata
Mesozoic orogenic belt
Cambrian to Triassic strata
Neoproterozoic-Cambrian
Meso-Neoproterozoic rocks
Archean-Paleoproterozoic rocks
Cretaceous normal fault
Mesozoic thrust fault
Triassic fold axis
Jurassic fold axis
Early Paleozoic and older fold axis
0 100 200km
108°E
112°E
114°E
(A)
90°E 110°E 130°E
0 500 1000km
40°N
Tarim Block
Tan-Lu fault
Qaidam
Qilian
Kunlun
North China Craton
Tibet Plateau
Songpan Ganzi block
Qinling
30°N
South China Craton
20°N
Figure 1B
90°E 100°E 110°E 120°E
(C)
117°
118°
0 10 20 km
Paleocurrents directions
Paleo-winds directions
28° 30'
Hengfeng
Shangrao
Yiyang
K2h
K2lh
K2t
28° 20'
Guixi
Yanshan
Yingtan
Quaternary
Townships
Sample location
Alluvial fan (K2h)
Desert center (K2t)
Desert margin (K2t)
Fluvial deposits (K2lh)

Figure 2

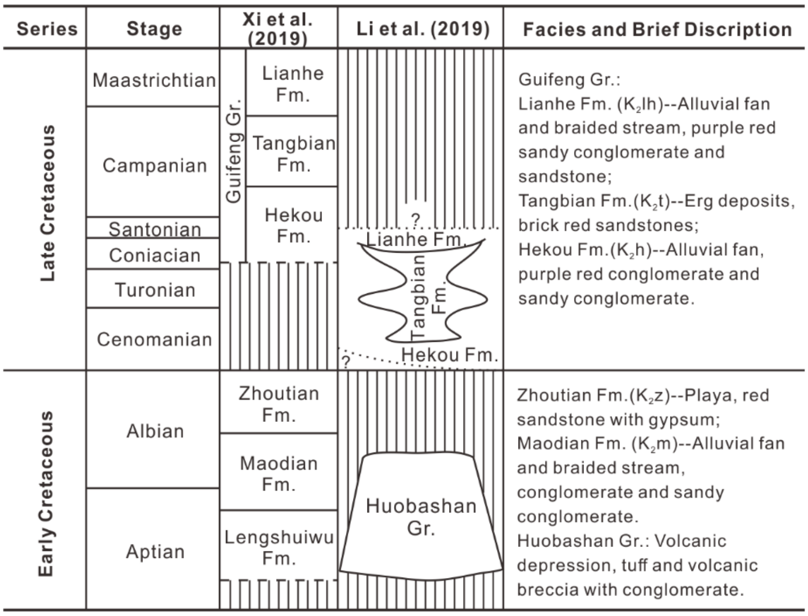

Figure 3

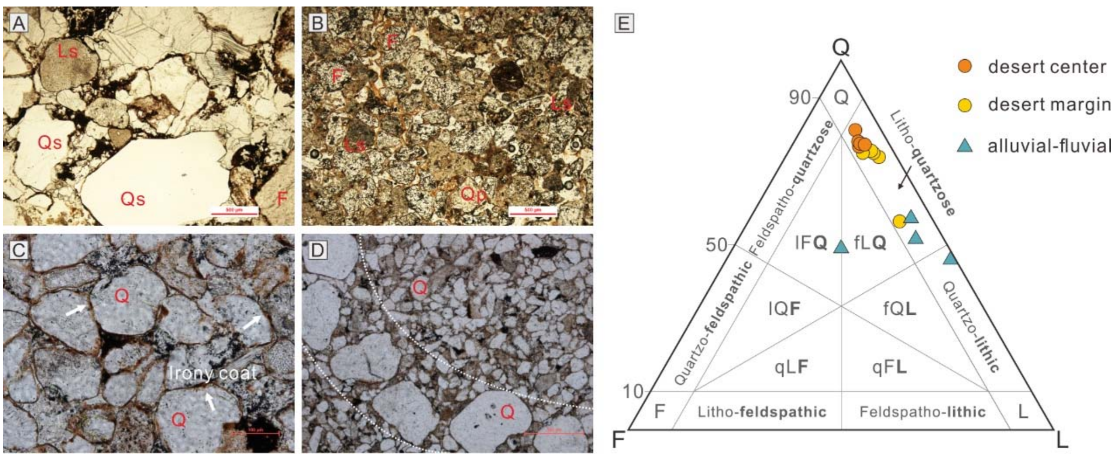

Figure 4

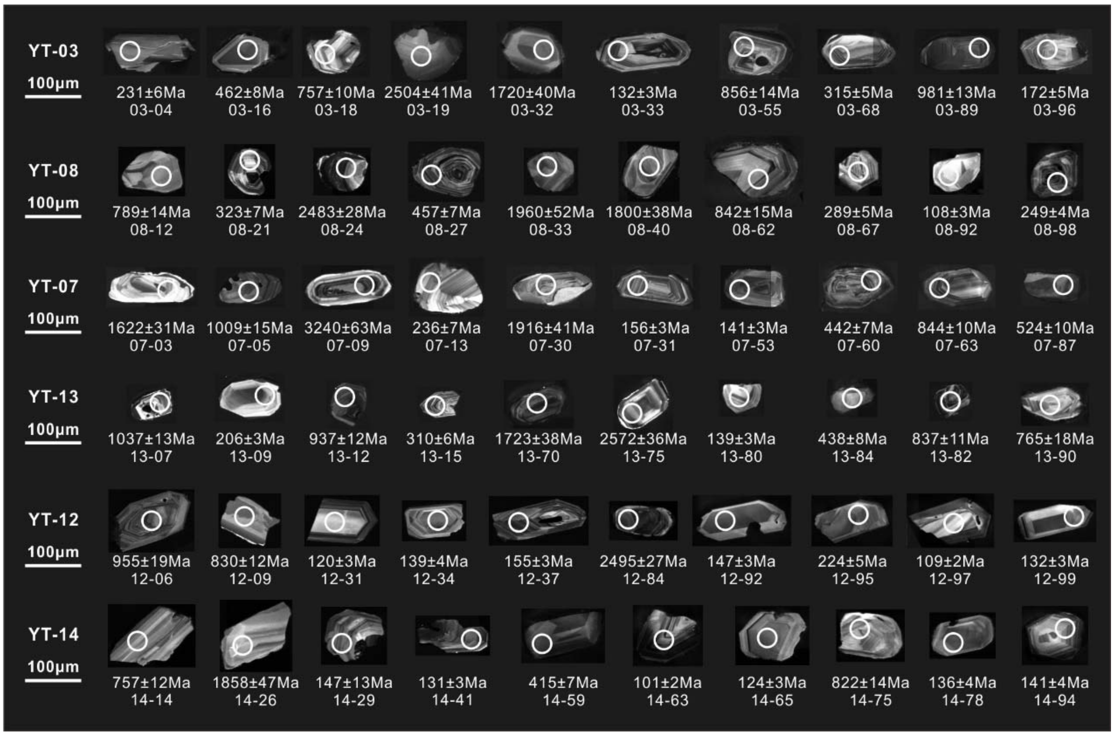
YT-03
100μm
231±6Ma 03-04
462±8Ma 03-16
757±10Ma 03-18
2504±41Ma 03-19
1720±40Ma 03-32
132±3Ma 03-33
856±14Ma 03-55
315±5Ma 03-68
981±13Ma 03-89
172±5Ma 03-96
YT-08
100μm
789±14Ma 08-12
323±7Ma 08-21
2483±28Ma 08-24
457±7Ma 08-27
1960±52Ma 08-33
1800±38Ma 08-40
842±15Ma 08-62
289±5Ma 08-67
108±3Ma 08-92
249±4Ma 08-98
YT-07
100μm
1622±31Ma 07-03
1009±15Ma 07-05
3240±63Ma 07-09
236±7Ma 07-13
1916±41Ma 07-30
156±3Ma 07-31
141±3Ma 07-53
442±7Ma 07-60
844±10Ma 07-63
524±10Ma 07-87
YT-13
100μm
1037±13Ma 13-07
206±3Ma 13-09
937±12Ma 13-12
310±6Ma 13-15
1723±38Ma 13-70
2572±36Ma 13-75
139±3Ma 13-80
438±8Ma 13-84
837±11Ma 13-82
765±18Ma 13-90
YT-12
100μm
955±19Ma 12-06
830±12Ma 12-09
120±3Ma 12-31
139±4Ma 12-34
155±3Ma 12-37
2495±27Ma 12-84
147±3Ma 12-92
224±5Ma 12-95
109±2Ma 12-97
132±3Ma 12-99
YT-14
100μm
757±12Ma 14-14
1858±47Ma 14-26
147±13Ma 14-29
131±3Ma 14-41
415±7Ma 14-59
101±2Ma 14-63
124±3Ma 14-65
822±14Ma 14-75
136±4Ma 14-78
141±4Ma 14-94

Figure 5

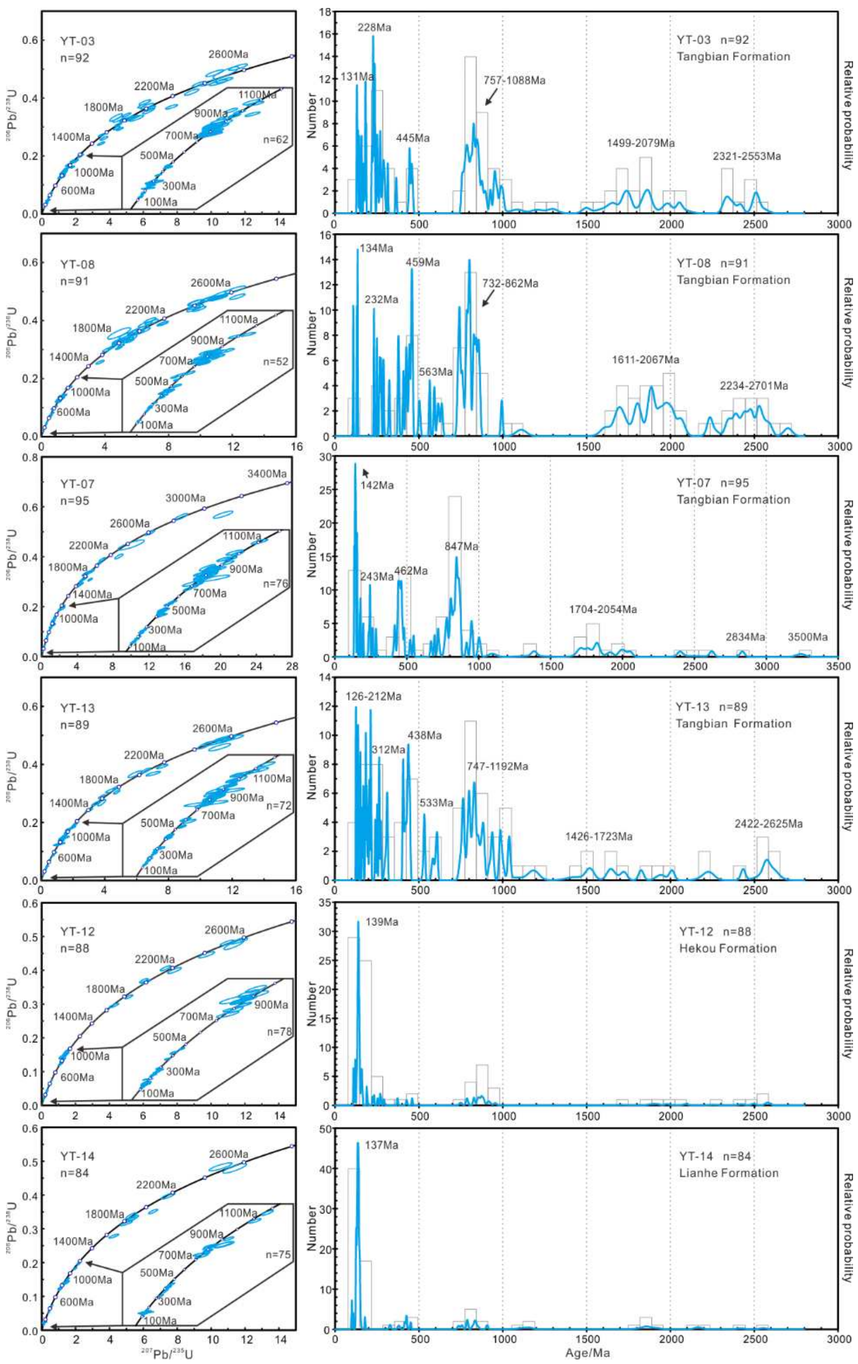

YT-03 n=92
YT-03 n=92 Tangbian Formation
228Ma
131Ma
445Ma
757-1088Ma
1499-2079Ma
2321-2553Ma
YT-08 n=91
YT-08 n=91 Tangbian Formation
134Ma
459Ma
232Ma
732-862Ma
563Ma
1611-2067Ma
2234-2701Ma
YT-07 n=95
YT-07 n=95 Tangbian Formation
142Ma
243Ma
462Ma
847Ma
1704-2054Ma
2834Ma
3500Ma
YT-13 n=89
YT-13 n=89 Tangbian Formation
126-212Ma
312Ma
438Ma
533Ma
747-1192Ma
1426-1723Ma
2422-2625Ma
YT-12 n=88
YT-12 n=88 Hekou Formation
139Ma
YT-14 n=84
YT-14 n=84 Lianhe Formation
137Ma
Number
Relative probability
Age/Ma

Figure 6

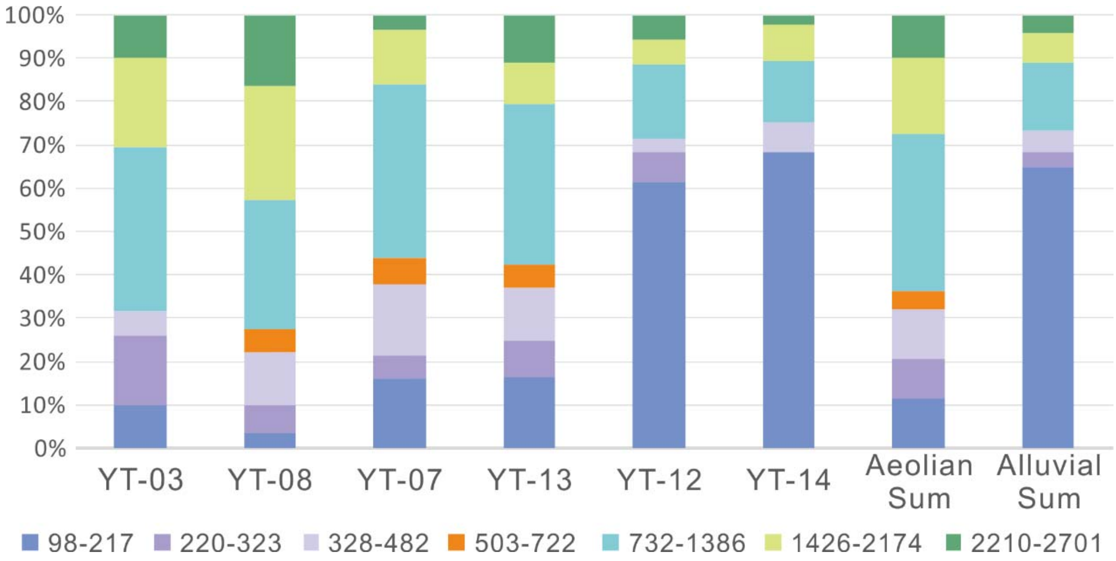
100%
90%
80%
70%
60%
50%
40%
30%
20%
10%
0%
YT-03
YT-08
YT-07
YT-13
YT-12
YT-14
Aeolian Sum
Alluvial Sum
98-217
220-323
328-482
503-722
732-1386
1426-2174
2210-2701

Figure 7

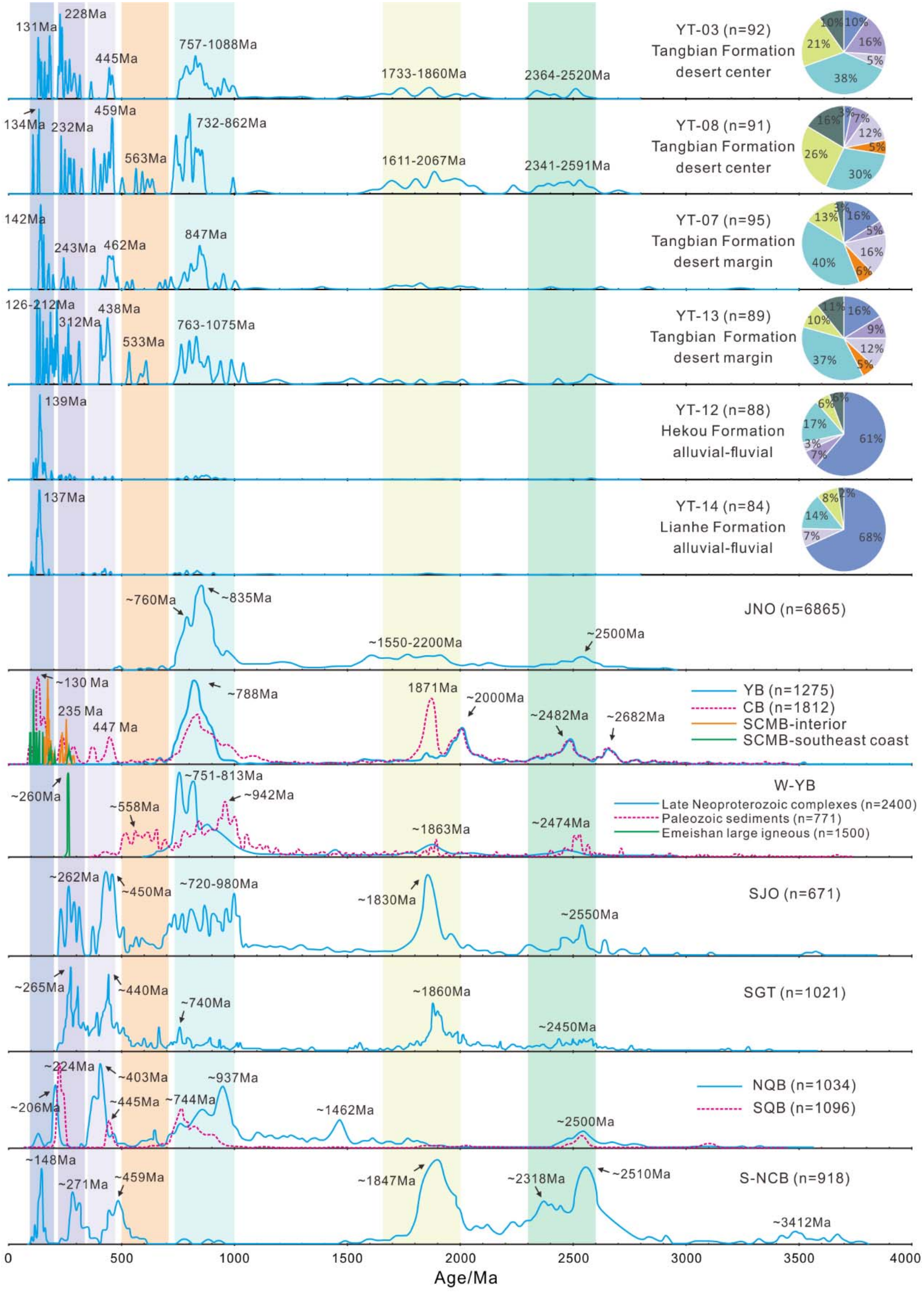

131Ma
228Ma
445Ma
757-1088Ma
1733-1860Ma
2364-2520Ma
YT-03 (n=92)
Tangbian Formation
desert center
134Ma
232Ma
459Ma
563Ma
732-862Ma
1611-2067Ma
2341-2591Ma
YT-08 (n=91)
Tangbian Formation
desert center
142Ma
243Ma
462Ma
847Ma
YT-07 (n=95)
Tangbian Formation
desert margin
126-212Ma
312Ma
438Ma
533Ma
763-1075Ma
YT-13 (n=89)
Tangbian Formation
desert margin
139Ma
YT-12 (n=88)
Hekou Formation
alluvial-fluvial
137Ma
YT-14 (n=84)
Lianhe Formation
alluvial-fluvial
~760Ma
~835Ma
~1550-2200Ma
~2500Ma
JNO (n=6865)
~130 Ma
235 Ma
447 Ma
~788Ma
1871Ma
~2000Ma
~2482Ma
~2682Ma
YB (n=1275)
CB (n=1812)
SCMB-interior
SCMB-southeast coast
~260Ma
~751-813Ma
~558Ma
~942Ma
~1863Ma
~2474Ma
W-YB
Late Neoproterozoic complexes (n=2400)
Paleozoic sediments (n=771)
Emeishan large igneous (n=1500)
~262Ma
~450Ma
~720-980Ma
~1830Ma
~2550Ma
SJO (n=671)
~265Ma
~440Ma
~740Ma
~1860Ma
~2450Ma
SGT (n=1021)
~224Ma
~403Ma
~937Ma
~206Ma
~445Ma
~744Ma
~1462Ma
~2500Ma
NQB (n=1034)
SQB (n=1096)
~148Ma
~271Ma
~459Ma
~1847Ma
~2318Ma
~2510Ma
~3412Ma
S-NCB (n=918)
0
500
1000
1500
2000
2500
3000
3500
4000
Age/Ma

Figure 8

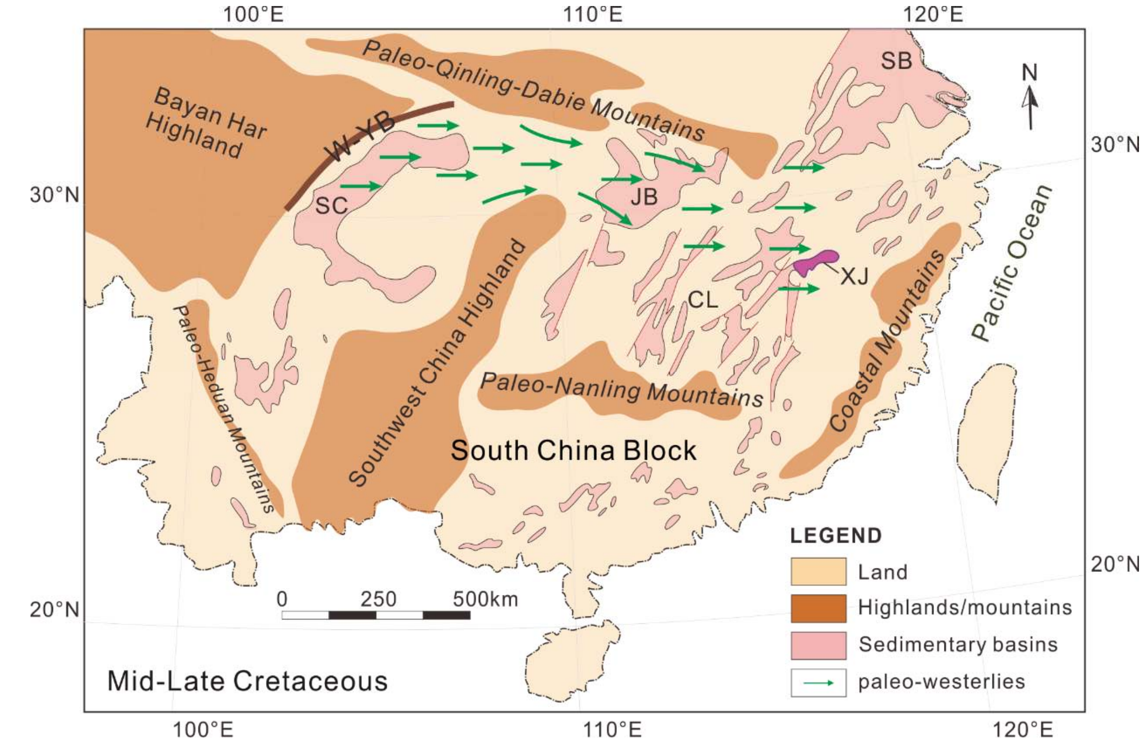

100°E
110°E
120°E
30°N
20°N
Bayan Har Highland
Paleo-Qinling-Dabie Mountains
W-YB
SC
JB
SB
N
CL
XJ
Pacific Ocean
Coastal Mountains
Southwest China Highland
Paleo-Heduan Mountains
Paleo-Nanling Mountains
South China Block
0 250 500km
LEGEND
Land
Highlands/mountains
Sedimentary basins
paleo-westerlies
Mid-Late Cretaceous

Table 1. Maximum depositional ages calculated from zircon U-Pb geochronology of sandstone samples from the Xinjiang Basin

Formation	Sample	Analyzed number of zircon grains	Maximum depositional age*	YDZ† (Ma)	YSG† (Ma)	YPP† (Ma)	YC1σ(2+)† (Ma)	YC2σ(3+)† (Ma)
K_2hl	YT-14	84	99.5	99+4.2/-10	98±4	100.8	99.5±3 (*n*=2)	102.3±3 (*n*=3)
K_2t	YT-03	92	131	129.6+4.8/-6.4	130±3	131.3	131±3 (*n*=2)	127±3 (*n*=3)
	YT-07	95	137	133.1+4.2/-9.8	134±3	141.8	137±4.3 (*n*=4)	140.2±3.8 (*n*=9)
	YT-08	91	132	108.3+6.3/-7.1	108±3	130.2	132±2.5 (*n*=2)	131.7±2.7 (*n*=3)
	YT-13	89	126	124.3+4.2/-4.5	125±2	126	126±2.5 (*n*=2)	129.7±2.7 (*n*=3)
K_2h	YT-12	88	109.5	108.5+3.3/-4.2	109±2	109.2	109.5±2 (*n*=2)	111.3±2 (*n*=3)

Note. *Maximum depositional age is determined by YC1σ(2+). †Different measures of youngest detrital zircon age after Dickinson and Gehrels (2009). YDZ—age calculated by the "youngest detrital zircon" routine of isoplot (Ludwig, 2008); YSG—youngest single detrital zircon age with 1σ uncertainty; YPP—youngest graphical detrital zircon age peak on an age-probability plot or age-distribution curve; YC1σ(2+)—weighted mean age of two or more youngest grain ages overlapping in age at 1σ; YC2σ(3+)—weighted mean age of three or more youngest grain ages overlapping in age at 2σ.

SUPPORTING INFORMATION

Appendix S1

Reconstruction of Palaeowind Directions for the Late Cretaceous Xinjiang Intermontane Desert

The aeolian sandstone with high-angle cross-bedding can be used as a proxy to reconstruct palaeowind direction (Jiang, 2018). The relationships between dune types and dominant directions of the effective winds are different. The mean cross-bed dip directions of barchan, barchanoid, and transverse dunes are parallel to the wind direction, especially the perfectly transverse dunes (Rubin and Carter, 2006). However, the cross-beds dip directions of oblique and longitudinal dunes are not parallel to the wind direction (Mountney, 2006; Rubin and Hunter, 1985). Rubin (1987) and Rubin and Carter (2006) presented a collection of computer-generated images of cross-bedding to distinguish the deposits of transverse, oblique and longitudinal bedforms. For the perfectly transverse dunes, dips have bilateral symmetry and dip directions of their cross-beds are distributed unimodally; for the oblique dunes, cross-bed dips are asymmetrically distributed; for the perfectly longitudinal dunes, dips have bilateral symmetry and dip directions of their cross-beds are often distributed bimodal (Rubin and Carter, 1987; Rubin and Carter, 2006).

In the Late Cretaceous Xinjiang intermontane desert, the azimuths of aeolian dune cross-beds were measured from 16 sections (Cao et al., 2020). As the South China Block rotated by 16.7 ± 5.0° in the mid-Cretaceous to Paleogene, these measured data have been corrected to the palaeo-direction. Sections 1, 3, 15, 16 are small-scale barchan dunes (Fig. S1A). Consisting of high-angle trough cross beddings, they are often less than 2 m in thickness and could be traced for only tens of meters in all directions. They are much smaller than the large-scale aeolian dunes and the dip directions of the cross-beds are variable (Fig. S2), which might be affected by the secondary winds, so that they are excluded from the reconstruction of the primary palaeowind direction. Their trough cross beddings have scoured bases and either symmetrical or asymmetrical axes. Sections 5, 9, 11, 12 are large-scale near-perfectly transverse dunes (Fig. S1B), parallel stacked and bounded by laterally extensive, very low-angle inclined bounding surfaces. Generally, the thickness is tens of meters, and their lateral distribution is several hundred meters. The compound forms are important components of the draa bedform and distributed only in the central desert. The dip directions of the cross-beds of these transverse dunes are consistent and unidirectional, orienting to ENE, which are parallel to the palaeowind (Fig. S2). Sections 2, 8, 13 are the large-scale longitudinal dunes. The dip directions of their cross-beds are in almost opposite directions (Fig. S2). Sections 4, 6, 7, 10, 14 are the large-scale complex aeolian dunes. They are a mix of transverse, oblique and longitudinal dunes. The dip directions of their cross-beds are multi-directional, so that they can not accurately reflect the palaeowind direction.

In conclusion, the large-scale near-perfectly transverse dunes are the ideal materials for the reconstruction of palaeowind direction, and results shows that the palaeowind blew from west-southwest to east-northeast, reflecting the influence of westerlies.

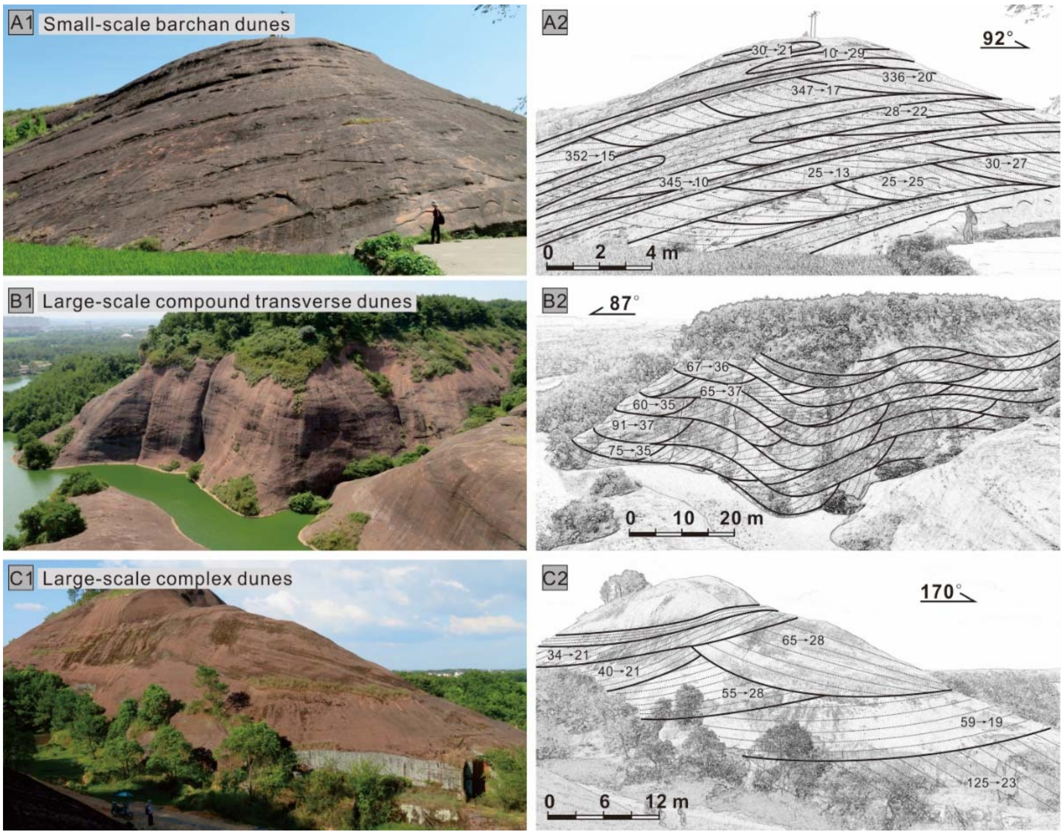

Fig. S1. Outcrops and line drawings of (A) small-scale barchan dunes, (B) large-scale compound transverse dunes and (C) large-scale complex dunes. Black lines represent aeolian surfaces (interdune migration surfaces, superimposition surfaces, and reactivation surfaces); and gray, dashed lines represent cross-stratifcation. The numbers before each arrow/after each arrow represent the azimuth/dip of the cross beddings. Modified from Cao et al., 2020.

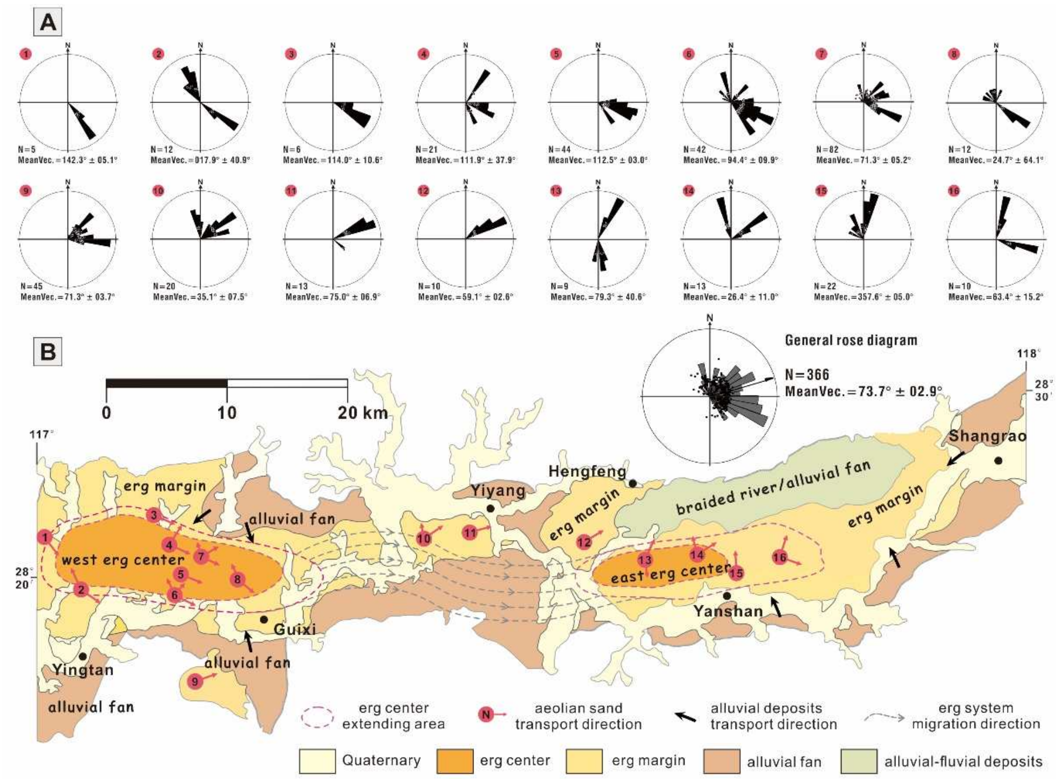

Fig. S2. Palaeogeographic map and palaeowind directions of the Tangbian Formation in the Xinjiang Basin during the Late Cretaceous. Modified from Cao et al., 2020.

REFERENCES

Cao, S., Zhang, L., Wang, C., Ma, J., Tan, J. and Zhang, Z. (2020) Sedimentological characteristics and aeolian architecture of a plausible intermountain erg system in Southeast China during the Late Cretaceous. *GSA Bulletin*, **132,** 2475-2488.

Jiang, Z. (2018) *Sedimentary dynamics of windfield-source-basin system: new concept for interpretation and prediction*. Springer.

Mountney, N.P. (2006) Eolian facies models. In: *Facies Models Revisited* (Ed R.G.W. H.W. Posamentier), **Special Publication**, pp. 19-83. Society for Economic Paleontologists and Mineralogists, Tulsa, Oklahoma.

Rubin, D.M. and Carter, C.L. (1987) *Cross-Bedding, Bedforms, and Paleocurrents*. SEPM Society for Sedimentary Geology.

Rubin, D.M. and Carter, C.L. (2006) *Cross-bedding, bedforms, and paleocurrents*. Society for Sedimentary Geology.

RUBIN, D.M. and HUNTER, R.E. (1985) Why deposits of longitudinal dunes are rarely recognized in the geologic record. *Sedimentology*, **32,** 147-157.

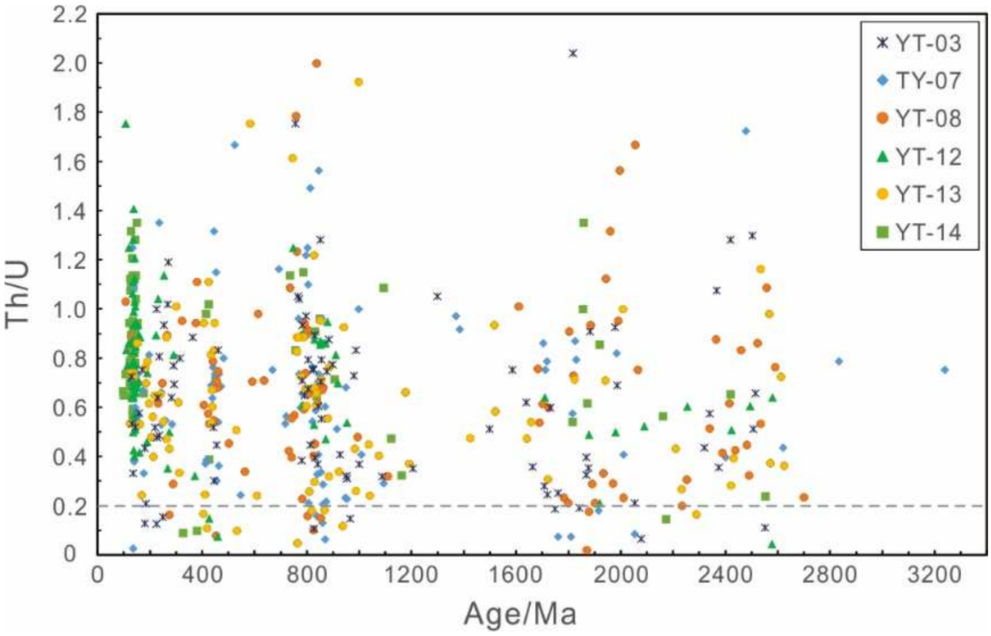

Fig. S3. Crossplot of Th/U ratios versus U–Pb ages of concordant detrital zircons from sandstones in the Xinjiang intermountain desert.

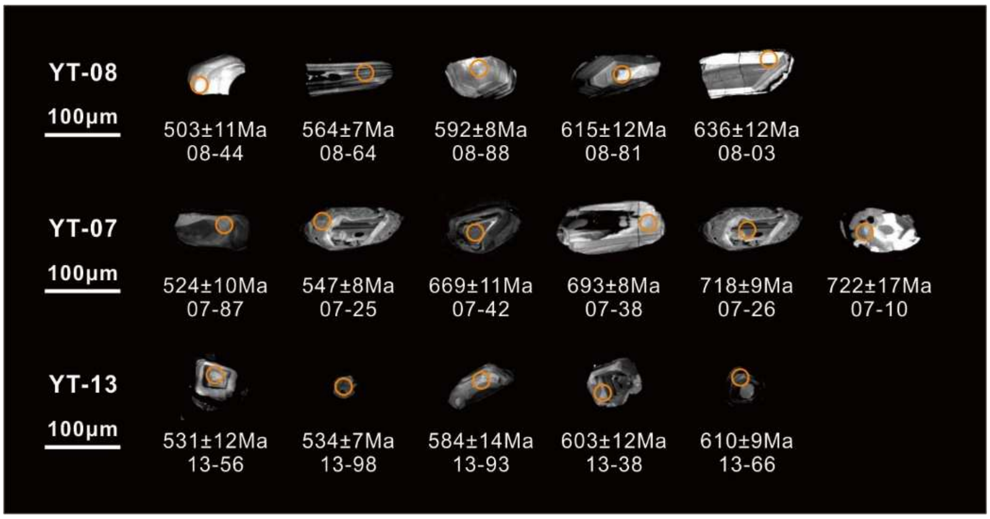

Fig. S4. Cathodoluminescence (CL) images of representative 503-722 Ma zircon grains from the Xinjiang intermountain desert. The small white circles show the sites for U–Pb age analyses and the ages (Ma). YT-08 was taken from aeolian sediments in the desert center, and YT-07 & YT-13 were taken from aeolian sediments in the desert margin.

Table S1. Location information of 14 sandstone samples throughout the Xinjiang Basin.

No.	Sample	Formation	Section	Subregion	Type	GPS	Technique
1	YT-03	K_2t	Xianrenshi	Desert center	Barchan dune	28°21'54"N 117° 09'59"E	Thin section LA-ICP-MS
2	YT-08	K_2t	Longyanshan	Desert center	Transverse dune	28°20'29"N 117° 08'54"E	Thin section LA-ICP-MS
3	JXY-17	K_2t	Zhiguangzhen	Desert center	Transverse dune	28°22′10″N 117°04′39″E	Thin section
4	JXY-18	K_2t	Yanqianpengjia	Desert center	Transverse dune	28°17′57″N 117°10′40″E	Thin section
5	JXY-25	K_2t	Nanyansi	Desert center	Barchan dune	28°16′27″N 117°10′40″E	Thin section
6	YT-07	K_2t	Hejiacun	Desert margin	Dry interdune	28°23'34"N; 117° 08'19"E	Thin section LA-ICP-MS
7	YT-13	K_2t	Yanshan	Desert margin	Barchan dune	28°19'21"N 117°42'17"E	Thin section LA-ICP-MS

8	JXY-09	K_2t	Zhongcun	Desert margin	Dry Interdune	28°23′34″N 117°08′19″E	Thin section
9	JXY-15	K_2t	Hongshichang	Desert margin	Barchan dune	28°22′02″N 117°14′09″E	Thin section
10	JXY-21	K_2t	Yinlingshi	Desert margin	Sandsheet	28°16′54″N 117°12′23″E	Thin section
11	YT-12	K_2h	Houzhang	Extra desert	alluvial	28°24'07"N 117°12'53"E	Thin section LA-ICP-MS
12	JXY-22	K_2h	Zhujiayuan	Extra desert	alluvial	28°23′33″N 117°15′34″	Thin section
13	YT-14	K_2lh	Daguyan	Extra desert	Fluvial	28°25'33"N 117°51'08"E	Thin section LA-ICP-MS
14	JXS-02	K_2lh	Wanjiazhu	Extra desert	Fluvial	E28°25′03″N 117°46′07″E	Thin section

Table S2. Laser ablation inductively coupled plasma spectrometry (LA-ICP-MS) data of detrital zircons from the Xinjiang intermontane desert in SE China.